



Populating the Upper Black Hole Mass Gap through Stellar Collisions in Young Star Clusters

Kyle Kremer^{1,2,3,11} , Mario Spera^{1,4,5} , Devin Becker^{1,6}, Sourav Chatterjee⁷ , Ugo N. Di Carlo^{5,8,9} , Giacomo Fragione¹ , Carl L. Rodriguez¹⁰ , Claire S. Ye¹ , and Frederic A. Rasio¹

¹ Center for Interdisciplinary Exploration & Research in Astrophysics (CIERA) and Department of Physics & Astronomy, Northwestern University, Evanston, IL 60208, USA; kkremer@caltech.edu

² TAPIR, California Institute of Technology, Pasadena, CA 91125, USA

³ The Observatories of the Carnegie Institution for Science, Pasadena, CA 91101, USA

⁴ Dipartimento di Fisica e Astronomia “G. Galilei”, University of Padova, Vicolo dell’Osservatorio 3, I-35122, Padova, Italy

⁵ INFN, Sezione di Padova, Via Marzolo 8, I-35131, Padova, Italy

⁶ Department of Physics and Astrophysics, DePaul University, Chicago, IL 60614, USA

⁷ Tata Institute of Fundamental Research, Homi Bhabha Road, Mumbai 400005, India

⁸ Università degli Studi dell’Insubria, Dipartimento di Scienza e Alta Tecnologia, Via Valleggio 11, I-22100, Como, Italy

⁹ INAF, Sezione di Padova, Vicolo dell’Osservatorio 5, I-35122, Padova, Italy

¹⁰ Harvard Institute for Theory and Computation, 60 Garden Street, Cambridge, MA 02138, USA

Received 2020 June 17; revised 2020 September 10; accepted 2020 September 15; published 2020 October 30

Abstract

Theoretical modeling of massive stars predicts a gap in the black hole (BH) mass function above $\sim 40\text{--}50 M_{\odot}$ for BHs formed through single star evolution, arising from (pulsational) pair-instability supernovae (PISNe). However, in dense star clusters, dynamical channels may exist that allow construction of BHs with masses in excess of those allowed from single star evolution. The detection of BHs in this so-called “upper-mass gap” would provide strong evidence for the dynamical processing of BHs prior to their eventual merger. Here, we explore in detail the formation of BHs with masses within or above the pair-instability gap through collisions of young massive stars in dense star clusters. We run a suite of 68 independent cluster simulations, exploring a variety of physical assumptions pertaining to growth through stellar collisions, including primordial cluster mass segregation and the efficiency of envelope stripping during collisions. We find that as many as $\sim 20\%$ of all BH progenitors undergo one or more collisions prior to stellar collapse and up to $\sim 1\%$ of all BHs reside within or above the pair-instability gap through the effects of these collisions. We show that these BHs readily go on to merge with other BHs in the cluster, creating a population of massive BH mergers at a rate that may compete with the “multiple-generation” merger channel described in other analyses. This has clear relevance for the formation of very massive BH binaries as recently detected by the Laser Interferometer Gravitational-Wave Observatory/Virgo in GW190521. Finally, we describe how stellar collisions in clusters may provide a unique pathway to PISNe and briefly discuss the expected rate of these events and other electromagnetic transients.

Unified Astronomy Thesaurus concepts: [Stellar mass black holes \(1611\)](#); [Gravitational waves \(678\)](#); [Globular star clusters \(656\)](#)

1. Introduction

The mass spectrum of stellar-mass black holes (BHs) is among the most hotly debated topics in modern astrophysics. This is driven in large part by the growing catalog of binary BH mergers detected as gravitational-wave (GW) sources by the Laser Interferometer Gravitational-Wave Observatory (LIGO)/Virgo (The LIGO Scientific Collaboration et al. 2019a) over the past few years, which have complemented earlier constraints upon BH masses obtained from observations of X-ray binaries (e.g., Bailyn et al. 1998; Özel et al. 2010; Farr et al. 2011; Corral-Santana et al. 2016). Over the coming years and decades, current (LIGO, Virgo, and the Kamioka Gravitational Wave Detector (KAGRA)) and future (e.g., the Laser Interferometer Space Antenna (LISA), the Einstein Telescope, and the Deci-Hertz Interferometer Gravitational wave Observatory (DECIGO)) GW detectors promise to provide unprecedented constraints upon the BH mass distribution. Thus, it is essential to advance our theoretical understanding of the various pathways through which stellar BHs may form.

Stellar-mass BHs are expected to form as the end products of the evolution of massive stars, with the final mass of the BH determined by two primary elements, both ripe with uncertainty: the mass of the progenitor star (and core-to-envelope mass ratio) just before core collapse, and the details of the subsequent supernova (SN) explosion. The pre-explosion progenitor mass depends crucially upon (metallicity-dependent) stellar winds (e.g., Vink et al. 2001). In regard to the SN explosion, a number of theoretical models have been proposed and implemented in various studies which yield varying effects upon the BH mass spectrum (e.g., Heger et al. 2003; Woosley et al. 2007; Belczynski et al. 2010; Mapelli et al. 2010; O’Connor & Ott 2011; Fryer et al. 2012; Spera et al. 2015; Belczynski et al. 2016a; Sukhbold et al. 2016; Ertl et al. 2016; Farmer et al. 2019).

Specifically, stars with helium cores in the mass range $\sim 45\text{--}135 M_{\odot}$ are expected to undergo so-called pair-instability supernovae (PISNe): after the onset of carbon burning the production of electron–positron pairs leads to a rapid loss of pressure and core contraction. This contraction triggers explosive burning of heavier elements leading to a runaway thermonuclear explosion (e.g., Fowler & Hoyle 1964; Rakavy & Shaviv 1967;

¹¹ NSF Astronomy & Astrophysics Postdoctoral Fellow.

Barkat et al. 1967; Fraley 1968). Stars with helium cores in the range $\sim 65\text{--}135 M_{\odot}$ are thought to be completely destroyed by the PISNe, leaving no remnant (e.g., Bond et al. 1984; Fryer et al. 2001; Chatzopoulos & Wheeler 2012). On the other hand, if a star builds a helium core in the range $\sim 45\text{--}65 M_{\odot}$, the pair instability is expected to trigger a series of strong pulsations that efficiently reduce the mass and entropy of helium and heavy elements until the pulsing activity has damped. The latter process is known as pulsational pair-instability supernovae (PPSNe; e.g., Heger & Woosley 2002; Woosley et al. 2007; Woosley 2017, 2019).

PISNe and PPSNe have a strong imprint upon the BH mass spectrum, as these processes are expected to yield a prominent “gap” in BH mass between roughly 40 and $120 M_{\odot}$ for BHs formed through single star evolution (e.g., Belczynski et al. 2016a; Spera & Mapelli 2017). While the upper and lower boundaries of this mass gap are uncertain and depend upon various assumptions concerning the evolution of massive stars (e.g., Belczynski et al. 2016a; Spera & Mapelli 2017; Woosley 2017; Giacobbo et al. 2018; Limongi & Chieffi 2018; Farmer et al. 2019; Marchant et al. 2019; Stevenson et al. 2019; Belczynski et al. 2020; Mapelli et al. 2020; Renzo et al. 2020), studies of the first few GW events seems to corroborate, in general, the theoretical predictions of this mass gap (Fishbach & Holz 2017; Talbot & Thrane 2018; The LIGO Scientific Collaboration et al. 2019a).

A number of recent studies have shown that formation channels outside the standard single star evolution pathway may in fact provide pathways for populating this mass gap. For example, primordial BHs formed through collapse of gravitational instabilities in the early universe may not be subject to the same constraints as BHs formed through stellar evolution and may therefore occupy the mass gap (e.g., Carr et al. 2016). Additionally, mass-gap BHs may be born through the merger of two smaller BHs (e.g., Miller & Hamilton 2002; McKernan et al. 2012; Rodriguez et al. 2018a, 2018b; Gerosa & Berti 2019; Antonini & Gieles 2020; McKernan et al. 2020).

Alternatively, heavy BHs may also be formed from the collapse of anomalously massive progenitor stars that form via stellar collisions or mergers of massive binaries. These collisions may occur particularly often in dense stellar environments such as young star clusters (e.g., Portegies Zwart et al. 2004; Gürkan et al. 2006; Giersz et al. 2015; Mapelli 2016). Such “collisional runaway” episodes have traditionally been touted as a formation channel for the elusive class of intermediate-mass BHs (IMBHs) with masses in the range $\sim 10^2\text{--}10^4 M_{\odot}$ (see, e.g., Greene et al. 2019, for a review). More recently, Spera et al. (2019), Di Carlo et al. (2019, 2020), and Banerjee (2020) revisited this topic in the specific context of the pair-instability mass gap and showed that stellar collisions/mergers in young clusters may also provide a viable pathway for creating BHs with masses forbidden by single star evolution.

The potential role of star-cluster dynamics in creating BHs with masses within and/or above the pair-instability gap is particularly noteworthy. Over the past decade, a growing number of stellar-mass BH candidates have been identified in the Milky Way globular clusters (GCs) through both X-ray/radio (Strader et al. 2012; Chomiuk et al. 2013; Miller-Jones et al. 2015; Shishkovsky et al. 2018) and dynamical measurements (Giesers et al. 2018, 2019), suggesting that at least some GCs retain populations of BHs at present (Kremer et al. 2019; Weatherford et al. 2018, 2020). This observational evidence has

been complemented by recent computational simulations of GCs, which have demonstrated that realistic clusters can naturally retain hundreds to thousands of BHs throughout their complete lifetimes (e.g., Morscher et al. 2015; Kremer et al. 2020). Additionally, it is now clear that BH populations play a significant role in shaping the long-term dynamical evolution and present-day structure of GCs (Merritt et al. 2004; Mackey et al. 2007, 2008; Breen & Hogg 2013; Peuten et al. 2016; Wang et al. 2016; Chatterjee et al. 2017b; Arca Sedda et al. 2018; Kremer et al. 2018, 2019; Zocchi et al. 2019; Antonini & Gieles 2020; Kremer et al. 2020).

Furthermore, the dynamical processes relevant to BHs in stellar clusters have emerged as a viable formation channel for binary BH mergers similar to those detected to date by LIGO/Virgo (e.g., Portegies Zwart & Mcmillan 2000; O’Leary et al. 2009; Banerjee et al. 2010; Rodriguez et al. 2015, 2016; Antonini & Rasio 2016; Askar et al. 2017; Chatterjee et al. 2017a, 2017b; Hoang et al. 2018; Samsing et al. 2018; Fragione & Kocsis 2018; Zevin et al. 2019).¹² Mergers involving BHs in the mass gap would have properties difficult (or impossible) to produce through isolated binary evolution. Thus, the detection of binary BH mergers with component masses within the pair-instability mass gap (for example the recent event GW190521; Abbott et al. 2020a, 2020b) may be strong evidence for the dynamical processing of BHs prior to their eventual merger.

In this analysis, we investigate in detail the formation of massive BHs through stellar collisions in dense star clusters. Di Carlo et al. (2019, 2020) explored this topic in the context of lower-mass clusters ($\approx 10^3\text{--}10^4 M_{\odot}$) and found that, depending on the assumed metallicity, as many as $\sim 5\%$ of all BHs in young star clusters can have masses in the pair-instability gap as a result of collisions of young massive stars. They also showed that mass-gap BHs efficiently acquire BH binary companions and merge through subsequent dynamical encounters, yielding a subpopulation of binary black hole (BBH) mergers detectable by LIGO/Virgo with at least one component in the mass gap.

Here, we examine the role of stellar collisions on BH formation in the previously unexplored massive cluster regime, exploring specifically clusters with masses comparable to the GCs observed in the Milky Way ($\approx 10^3\text{--}10^6 M_{\odot}$; Harris 1996). This is a critical addition to previous literature on the topic, given that GCs and their progenitors may account for a large fraction of the overall BBH merger rate in the local universe (e.g., Rodriguez & Loeb 2018; Kremer et al. 2020).

We describe our computational methods for modeling dense star clusters in Section 2. In Section 3, we discuss the results of our simulations, describing specifically the various evolutionary outcomes for massive stars undergoing collisions in star clusters. We also discuss the long-term fate of the massive BHs that form through collisions, in particular investigating the possibility of BBH mergers. In Section 4, we discuss implications for GW astronomy, in particular compared to the recently detected upper-mass-gap event GW190521. In Section 5, we discuss briefly the

¹² In addition to dynamical formation in dense star clusters, a number of other binary BH formation channels have been proposed, including isolated massive binary evolution (e.g., Dominik et al. 2012, 2013; Belczynski et al. 2016b, 2016a), GW capture of primordial BHs (e.g., Bird et al. 2016; Sasaki et al. 2016), secular interactions in hierarchical triple systems (e.g., Antonini & Rasio 2016; Antonini et al. 2017; Silsbee & Tremaine 2017; Liu & Lai 2017; Hoang et al. 2018; Leigh et al. 2018; Fragione et al. 2019a; Fragione & Kocsis 2019; Fragione et al. 2019b; Rodriguez & Antonini 2018), and active galactic nuclei disks (e.g., McKernan et al. 2012; Secunda et al. 2019; Yang et al. 2019; McKernan et al. 2020).

cosmological rates of PISNe and other electromagnetic transients identified in our cluster simulations. We discuss our results and conclude in Section 6.

2. Modeling Cluster Evolution

We use CMC (Cluster Monte Carlo) to model the evolution of stellar clusters. CMC is a distributed-memory parallelized Hénon-type Monte Carlo code that includes prescriptions for various physical processes relevant to the problem at hand, including two-body relaxation, up-to-date stellar/binary evolution from the population synthesis code COSMIC (Breivik et al. 2020), direct integration of small- N resonant encounters (using the `fewbody` package; Fregeau et al. 2004), tidal mass loss (Chatterjee et al. 2010), and stellar collisions (Fregeau & Rasio 2007). For a recent review of the computational method of CMC, see Kremer et al. (2020) and references therein. Here, we make several changes to CMC to explore the particular subject of massive star collisions and implications for the formation of massive BHs. We summarize these changes below:

Primordial mass segregation. Observations of many young massive clusters (YMCs) show an increased concentration of massive stars near the cluster centers (e.g., Hillenbrand 1997; Hillenbrand & Hartmann 1998; Fischer et al. 1998; Gouliermis et al. 2004; Stolte et al. 2006). The origin of this mass segregation is uncertain. Mass segregation is known to be a natural feature of self-gravitating systems driven by two-body relaxation (e.g., Spitzer 1987; Heggie & Hut 2003). However, mass segregation is observed in many YMCs with ages much less than their relaxation times, suggesting that it may in fact be a primordial feature of at least some clusters. Primordial mass segregation has been proposed to result, for example, from the preferential formation of massive stars in the densest regions of the molecular cloud (e.g., Murray & Lin 1996) or by gas accretion during the initial phases of star formation (Bonnell & Bate 2006).

A number of recent studies have explored the effect of primordial mass segregation on the formation of massive stars through collisional runaway (e.g., Gürkan et al. 2004; Ardi et al. 2008; Goswami et al. 2012). Such runaways have been proposed as a potential formation channel for IMBHs (e.g., Portegies Zwart & McMillan 2002a; Freitag et al. 2006). To investigate these potential effects, we run simulations both with and without primordial mass segregation. We adopt the recipe of Baumgardt et al. (2008) to create primordial mass-segregated clusters in virial equilibrium. In this recipe, stars are sorted such that (for a fixed number density profile) the most massive stars have, on average, the lowest specific energy. For illustration, in Figure 1, we show the average stellar-mass profile (top panel) and mass density profile (bottom panel) for two clusters with identical particle numbers and initial mass functions (IMFs) with and without primordial mass segregation. Here we show radial position in units of the cluster virial radius, $r_v = GM_c^2 / (2U)$, where M_c is the cluster mass and U is the total cluster potential energy. See also Goswami et al. (2012) for a recent detailed examination of the effects of primordial mass segregation using CMC.

Initial stellar binaries and three-body binary formation. In order to isolate the effect of dynamical collisions on stellar growth, we assume zero stellar binaries in all simulations in this study. As a result, all stellar collisions considered in this study occur through single–single encounters in which the pericenter

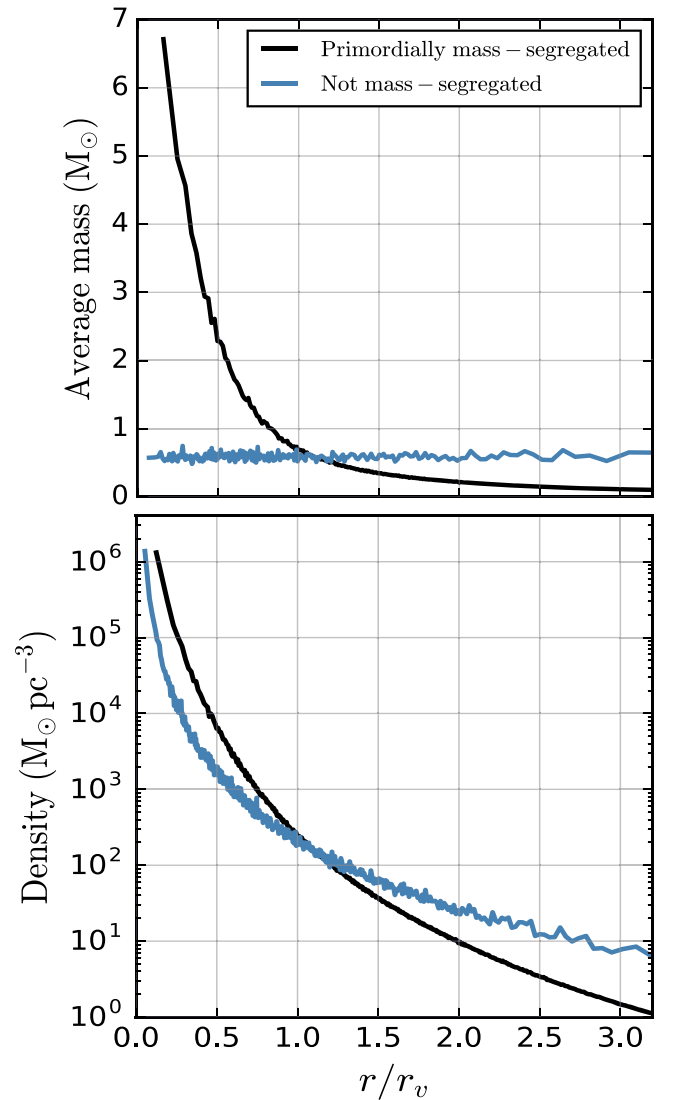


Figure 1. Top panel: average stellar-mass profile vs. radius (in units of initial virial radius) for a non-mass-segregated cluster (blue) and a primordially mass-segregated cluster (black) initialized using the recipe of Baumgardt et al. (2008). Bottom panel: density profile for the same two models.

distance of the pair of stars at closest approach is less than the sum of radii of the pair ($r_p \leq R_1 + R_2$). See Fregeau & Rasio (2007) for a detailed explanation of the treatment of single–single collisions in CMC. Recent analyses have shown that binary evolution processes (e.g., mass transfer, common envelope, tides) can play an important role in the formation of massive BHs both in the field and in star clusters (e.g., Spera et al. 2019; Di Carlo et al. 2019, 2020). Thus, by not including stellar binaries, the results of this study may be viewed as a lower limit on the formation rate of massive BHs in dense star clusters.

Although we do not include stellar binaries in our models, once BHs form, we do allow BH binaries to form through three-body binary formation (e.g., Heggie & Hut 2003). We follow the formalism outlined in Morscher et al. (2013), allowing BH binaries to form with $\eta \geq 2 = \eta_{\min}$, where η is the binary hardness ratio (binary binding energy to background star kinetic energy). The formation of BH binaries through this mechanism is essential for the ejection of BHs throughout the

cluster evolution and also the formation of GW sources (see Kremer et al. 2020, for a review).

Treatment of stellar collision products. The ultimate fate of a stellar collision product depends upon the details of the collision, which in turn depend on the internal structures of the two colliding stars. For collisions of two main-sequence (MS) stars, we adopt the so-called “sticky sphere” approximation where we assume no mass is lost during the collision itself such that M_3 , the mass of the collision product, is simply equal to the sum of the masses of the two colliding stars, $M_1 + M_2$. The stellar age of the new main-sequence star is given by

$$t_3 = f_{\text{rejuv}} \frac{t_{\text{MS3}}}{M_3} \left(\frac{M_1 t_1}{t_{\text{MS1}}} + \frac{M_2 t_2}{t_{\text{MS2}}} \right), \quad (1)$$

where t_{MS1} , t_{MS2} , and t_{MS3} are the MS lifetimes of the two collision components and the collision product, respectively, and t_1 and t_2 are the stellar ages of the two collision components at the time of collision. f_{rejuv} is a factor that determines the amount of rejuvenation the collision product experiences through mixing. In reality, this factor depends upon the internal structure of the two stars as well as the nature of the collision (i.e., the impact parameter and velocity at infinity). In original BSE (Hurley et al. 2002), a fixed value of 0.1 is assumed for f_{rejuv} . However, in many instances this likely leads to over-rejuvenation of the collision product. Therefore we adopt $f_{\text{rejuv}} = 1$ as our default value (see also Breivik et al. 2020, for discussion).

If on the other hand, at least one of the collision components is a giant, the complete mixing scenario relevant for MS–MS collisions is no longer applicable and instead the collision is qualitatively more similar to a common envelope episode where the cores of the two stars inspiral within an envelope of more loosely bound material. In this case, it is less clear whether the sticky sphere assumption is appropriate. Therefore, we adopt two different prescriptions for collisions involving giant stars that bracket the range of expected outcomes. As an upper-limit case, we assume sticky sphere collisions where the collision product’s total mass is again computed as $M_3 = M_1 + M_2$ and the core mass is computed as $M_{c,3} = M_{c,1} + M_{c,2}$ (note that we assume $M_c = 0$ for main-sequence stars). As a lower limit case, we assume that the envelopes of giant stars are completely unbound through the collision process. In this limit, in the case of a giant–main-sequence collision, $M_3 = M_{c,1} + M_2$ and $M_{c,3} = M_{c,1}$, such that the collision product is a giant. In the case of a giant–giant collision, $M_3 = M_{c,3} = M_{c,1} + M_{c,2}$ such that the collision product is a naked helium core.¹³

Collisional runaways. Clusters with sufficiently high initial densities may lead to high stellar collision rates and potentially to the formation of a very massive star ($M \gtrsim 1000 M_\odot$) within the first few Myr before the stars undergo core-collapse supernovae. A number of analyses have shown that these very massive stars may have important implications for the formation of IMBHs (e.g., Ebisuzaki et al. 2001; Portegies Zwart & McMillan 2002b;

Gürkan et al. 2004; Freitag et al. 2006; Portegies Zwart et al. 2010; Goswami et al. 2012). For clusters that are primordially mass segregated, the onset of these collisional runaways may be even more likely (e.g., Goswami et al. 2012).

Treatment of the various physical processes relevant in the presence of a very massive star (and/or an IMBH) is, at present, beyond the computational scope of CMC. Therefore, if a star of mass $\geq 1000 M_\odot$ forms through stellar collisions, we simply stop the simulation and record the outcome as a collisional runaway. Note that this assumed $1000 M_\odot$ threshold is chosen to be roughly consistent with the findings of Portegies Zwart & McMillan (2002a), which showed that the products of collisional runaways can reach masses of up to roughly 0.1% of the total cluster mass.

Compact object formation. We adopt the (metallicity-dependent) stellar wind prescriptions of Vink et al. (2001) to determine the final stellar mass at the moment of core collapse. We use the “delayed” SNe explosion models (Fryer et al. 2012) to compute neutron star and BH masses modified to include prescriptions for PPSNe and PISNe. Following Belczynski et al. (2016a), we assume that any star with a pre-explosion helium core mass in the range $45\text{--}65 M_\odot$ will undergo pulsations that eject large amounts of the hydrogen envelope such that the final stellar mass at the time of core collapse is $45 M_\odot$. In this case, stars that undergo PPSNe are assumed to yield BHs of mass $40.5 M_\odot$ (we assume that 10% of the final core mass is lost through the conversion of baryonic matter to gravitational matter at the moment of collapse, such that the final remnant mass is 90% of the pre-explosion core mass). We assume stars with pre-explosion core masses in the range $65\text{--}135 M_\odot$ undergo PISNe and no compact remnant is formed. Stars with core masses in excess of $135 M_\odot$ are assumed to undergo direct collapse to a BH, such that the BH mass is equal to 90% of the pre-explosion *total* stellar mass, again accounting for 10% mass loss in conversion from baryonic to gravitational matter.¹⁴

BH and neutron star natal kicks are computed as in Kremer et al. (2020). We assume all BHs are born with zero spin (dimensionless spin parameter $a = 0$; Fuller & Ma 2019) and also assume that BHs can be spun up only through mergers with other BHs (although see Section 6 for discussion of alternative possibilities). In the event of a binary BH merger, we compute the spin (as well as mass and GW recoil kick) of the new BH using the method described in Rodriguez et al. (2018b), which in turn implements phenomenological fits to numerical and analytic relativity calculations (Campanelli et al. 2007; González et al. 2007; Lousto & Zlochower 2008, 2013; Barausse & Rezzolla 2009; Lousto et al. 2012; Gerosa & Kesden 2016).

In all models we assume $N = 8 \times 10^5$ stars at birth with masses drawn from an IMF ranging from $0.08\text{--}150 M_\odot$ with slopes following Kroupa (2001). We assume a metallicity of $Z = 0.002$ ($0.1 Z_\odot$) and adopt a fixed galactocentric distance of 20 kpc in a Milky Way–like galactic potential. In order to explore the effect of initial cluster density upon the stellar collision process, we vary the initial cluster virial radius: $r_v = 0.8, 0.9, 1, 1.1, \text{ and } 1.2$ pc. We turn on and off primordial mass segregation and also explore the upper and lower limit

¹³ A naked helium star (stellar type $k = 7$) is defined in standard BSE to have $M_c = 0$ (Hurley et al. 2002). If (in the lower limit case where we assume giant envelopes are ejected) a helium star (with mass M_1) undergoes a subsequent collision with a giant of mass M_2 and core mass $M_{c,2}$, we assume a new naked helium star is formed with total mass $M_3 = M_1 + M_{c,2}$ and core mass $M_{c,3} = 0$. We acknowledge that this simple treatment may miss subtleties associated with such collisions. However, because the radius of a naked helium star is small and the lifetime short, such collisions are rare, thus a more detailed treatment will not have a significant effect upon our results.

¹⁴ We note that the stellar evolution of very massive stars may be quite different from that of lower-mass stars (e.g., Chen et al. 2015). Thus, a more detailed study may implement alternative prescriptions for massive star evolution.

cases for giant collisions as described above. This yields a grid of $5 \times 2 \times 2 = 20$ simulations. To increase the statistical robustness of our results, we perform three to five independent simulations of each set of initial parameters, giving us 68 simulations in total. As we are interested primarily in exploring the imprint of stellar collisions on the BH mass spectrum, we run each simulation for only 30 Myr or until a collisional runaway occurs (the most massive star in the simulation grows to $\geq 1000 M_{\odot}$; see Section 2). Table 1 includes a complete list of all simulations in this study.

3. Results

In this section we describe the results in the context of the formation of BHs in the upper-mass gap. In Section 3.1 we describe the typical formation pathways to such objects and in Section 3.2 we describe the overall features of our complete set of simulations.

3.1. Evolutionary Outcomes from Massive Stellar Collisions

Here, we describe three distinct evolutionary outcomes for massive stars that undergo one or more collisions before stellar core collapse. Each of these outcomes is uniquely dependent upon stellar collisions and will never occur through single star evolution for the assumed IMF.¹⁵

In Figure 2 we show the stellar evolution for a characteristic example of each of the three outcomes (all taken from simulation 2c in Table 1, chosen simply because this simulation produces the full range of outcomes). In the top panel, we show the evolution of the total stellar mass up to the moment of stellar core collapse. Here, each of the filled circles denotes a collision event. In the bottom panel, we show the core mass versus time. The blue (gray) shaded regions mark the mass ranges where PISNe (PPSNe) are assumed to operate. In Figure 3, we provide cartoon illustrations of the collision sequence for each of the three outcomes shown in Figure 2. We provide further detail on each collision event in the tables in the Appendix.

Below, we summarize each of these three collision outcomes:

1. *BH in the pair-instability mass gap.* As described in Spera et al. (2019) and Di Carlo et al. (2019, 2020), if a massive star on the giant branch (i.e., it has a well-developed helium core) undergoes a collision/merger with a second non-evolved star (i.e., a star on the main sequence), the result may be an evolved star with an oversized hydrogen envelope. In particular, if the core mass of this star remains below the minimum mass for PPSN (here assumed to be $45 M_{\odot}$) and if the star retains a significant fraction of its recently acquired oversized envelope, the ultimate result may be a BH with a mass occupying the upper-mass gap. The green curves in Figure 2 illustrate a typical sequence leading to this outcome. See also the left-hand panel of Figure 3. In total, this outcome occurs three times in simulation 2c.

2. *PISNe.* The most massive stars drawn from the assumed IMF of our simulations is $150 M_{\odot}$. If left unperturbed, such a star will develop a pre-explosion core mass of just under $50 M_{\odot}$, falling within the mass range assumed to be subject to

PPSNe for our assumed metallicity (Vink et al. 2001; Breivik et al. 2020). Thus, for single star evolution alone, PISNe will never occur for our assumed IMF. However, if while on the giant branch, such a massive star undergoes one or more collisions with other giants with similarly massive cores, then the core of the collision product may grow sufficiently to fall in the range assumed to undergo a PISNe. In this case, no remnant is formed. The dark blue curve in Figure 2 illustrates a typical sequence leading to this outcome. See also the right-hand panel of Figure 3. In total, this outcome occurs five times in simulation 2c. We discuss PISNe in more detail in Section 5.

3. *Direct collapse and IMBH formation.* In the event of multiple collisions, the core may grow sufficiently to exceed the maximum core mass assumed to undergo PISNe in which case we assume a direct collapse results. BHs formed through this channel have masses in excess of $\sim 120 M_{\odot}$ and are generally placed in the class of so-called IMBHs.¹⁶ The light blue curve in Figure 2 illustrates the formation of an IMBH. See also the middle panel of Figure 3.

In the event of a collisional runaway, very massive stars in excess of $\sim 1000 M_{\odot}$ may form yielding similarly massive IMBHs (e.g., Gürkan et al. 2004; Ardi et al. 2008; Goswami et al. 2012; Giersz et al. 2015). A collisional runaway is generally expected to occur if the core mass segregation timescale of massive stars time is less than the stellar lifetime of the massive stars ($t \sim 3\text{--}5$ Myr; e.g., Gürkan et al. 2004). We identify collisional runaways in three of our simulations (1a, 1b, and 1c; see Table 1). Not surprisingly, these three models have the smallest initial r_v (0.8 pc) and therefore the shortest central relaxation times, ideal for triggering collisional runaways. In simulation 6d (also $r_v = 0.8$ pc but not assuming primordial mass segregation as in the former three runs) a $623 M_{\odot}$ IMBH (roughly $700 M_{\odot}$ pre-collapse progenitor) forms. This object is indeed analogous to the cases in simulations 1a, 1b, and 1c, but does not meet our (admittedly arbitrary) $1000 M_{\odot}$ requirement for labeling a collisional runaway. In the Appendix, we list full collision histories for each of the three collisional runaways.

3.2. Population Demographics

Column 5 of Table 1 shows the total number of BHs formed and retained at birth in each simulation and column 6 shows the number of these BHs that were formed through stellar collisions. As shown, we find that as many as 20% of all BHs in a typical cluster may have undergone at least one collision prior to collapse. Thus, stellar collisions may play a significant general role in BH formation in GCs. Columns 7–10 of Table 1 list the total number of BHs formed through PPSNe (assumed to yield BH masses of exactly $40.5 M_{\odot}$), the number of PISNe, the total number of BHs with masses in the pair-instability gap ($40.5\text{--}120 M_{\odot}$) formed through stellar collisions (see the left-hand panel of Figure 3), and the number of IMBHs with masses in excess of $120 M_{\odot}$. In addition, column 11 lists the mass of the largest BH formed in each simulation.

¹⁵ In addition to the three discussed outcomes, collisions may also lead to outcomes degenerate with those occurring through single star evolution (i.e., formation of BHs below the pair-instability gap or BHs that form through PPSNe). We discuss these briefly in Section 3.2.

¹⁶ The term IMBH is generally used to refer to the class of BHs of mass $\sim 10^2\text{--}10^5 M_{\odot}$ that bridge the divide between stellar-mass BHs ($M \lesssim 50 M_{\odot}$; i.e., upper limit associated with PPSNe) and supermassive BHs ($M \gtrsim 10^5 M_{\odot}$). In this analysis, we use the term “pair-instability gap” or “upper-mass-gap” BH to denote those BHs occupying the gap from $\sim 40\text{--}120 M_{\odot}$ expected from PPSNe and use the term “IMBH” to denote the specific class of massive BHs that form through direct collapse above the PISNe boundary.

Table 1
List of Cluster Simulations

Model	r_i (pc)	Prim. MS	Giant Coll.	N_{BH}	$N_{\text{BH, coll}}$	N_{PPSN}	N_{PISN}	$40.5 < M_{\text{BH}} < 120 M_{\odot}$	$M_{\text{BH}} > 120 M_{\odot}$	Max BH mass
1a	0.8	y	SS					Runaway at $t = 3.62$ Myr		
1b	0.8	y	SS					Runaway at $t = 3.57$ Myr		
1c	0.8	y	SS					Runaway at $t = 3.71$ Myr		
2a	0.9	y	SS	2217	109	72	4	7	0	94.2
2b	0.9	y	SS	2205	102	68	8	3	1	168.0
2c	0.9	y	SS	2221	119	66	5	3	1	328.1
2d	0.9	y	SS	2232	114	72	3	4	0	72.5
3a	1	y	SS	2236	72	78	2	3	0	66.1
3b	1	y	SS	2243	75	75	5	0	0	40.5
3c	1	y	SS	2237	76	70	2	1	2	202.4
3d	1	y	SS	2240	87	78	0	2	0	70.1
3e	1	y	SS	2240	103	79	2	2	0	69.6
4a	1.1	y	SS	2247	59	74	1	1	0	40.7
4b	1.1	y	SS	2255	68	79	0	1	0	41.4
4c	1.1	y	SS	2253	59	76	0	1	0	66.7
5a	1.2	y	SS	2256	42	73	1	1	0	45.4
5b	1.2	y	SS	2253	48	75	0	1	0	56.0
5c	1.2	y	SS	2243	51	73	4	2	0	85.0
5d	1.2	y	SS	2252	49	74	1	0	0	40.5
6a	0.8	n	SS	2246	382	62	0	3	0	64.8
6b	0.8	n	SS	2239	360	65	0	4	1	207.7
6c	0.8	n	SS	2222	349	69	3	2	1	230.5
6d	0.8	n	SS	2227	368	74	2	1	1	623.7
7a	0.9	n	SS	2247	286	71	3	2	0	55.8
7b	0.9	n	SS	2248	307	73	1	2	0	50.4
7c	0.9	n	SS	2256	288	68	2	0	0	40.5
8a	1	n	SS	2258	240	72	0	0	0	40.5
8b	1	n	SS	2256	235	68	0	0	0	40.5
8c	1	n	SS	2253	232	74	0	1	0	75.7
8d	1	n	SS	2258	240	74	0	0	0	40.5
9a	1.1	n	SS	2257	190	75	0	0	0	40.5
9b	1.1	n	SS	2257	188	76	0	1	0	53.5
9c	1.1	n	SS	2257	175	77	0	2	0	53.0
9d	1.1	n	SS	2256	193	75	0	0	0	40.5
10a	1.2	n	SS	2261	156	76	0	0	0	40.5
10b	1.2	n	SS	2256	161	74	1	0	0	40.5
10c	1.2	n	SS	2258	141	76	0	0	0	40.5
10d	1.2	n	SS	2257	162	76	0	0	0	40.5
11a	0.8	y	EE	2186	140	38	0	3	0	70.0
11b	0.8	y	EE	2202	138	43	0	4	0	67.3
11c	0.8	y	EE	2203	147	35	0	2	0	79.8
12a	0.9	y	EE	2225	115	51	0	2	0	70.6
12b	0.9	y	EE	2231	102	59	0	1	0	61.0
12c	0.9	y	EE	2213	102	53	0	0	0	40.5
13a	1	y	EE	2235	85	60	0	2	0	59.8
13b	1	y	EE	2239	78	60	0	0	0	40.5
13c	1	y	EE	2235	81	55	0	0	0	40.5
14a	1.1	y	EE	2243	63	63	0	2	0	74.2
14b	1.1	y	EE	2241	67	60	0	1	0	65.4
14c	1.1	y	EE	2244	67	63	0	3	0	65.0
15a	1.2	y	EE	2244	67	62	0	0	0	40.5
15b	1.2	y	EE	2248	53	57	0	0	0	40.5
15c	1.2	y	EE	2251	44	67	0	0	0	40.5
16a	0.8	n	EE	2235	344	25	0	0	0	40.5

Table 1
(Continued)

Model	r_i (pc)	Prim. MS	Giant Coll.	N_{BH}	$N_{\text{BH, coll}}$	N_{PPSN}	N_{PISN}	$40.5 < M_{\text{BH}} < 120 M_{\odot}$	$M_{\text{BH}} > 120 M_{\odot}$	Max BH mass
16b	0.8	n	EE	2244	391	20	0	0	0	40.5
16c	0.8	n	EE	2239	344	22	0	0	0	40.5
17a	0.9	n	EE	2247	290	34	0	0	0	40.5
17b	0.9	n	EE	2244	312	23	0	0	0	40.5
17c	0.9	n	EE	2249	295	31	0	0	0	40.5
18a	1	n	EE	2250	228	33	0	0	0	40.5
18b	1	n	EE	2246	220	38	0	0	0	40.5
18c	1	n	EE	2251	236	28	0	0	0	40.5
19a	1.1	n	EE	2253	170	48	0	0	0	40.5
19b	1.1	n	EE	2252	182	44	0	0	0	40.5
19c	1.1	n	EE	2252	160	53	0	0	0	40.5
20a	1.2	n	EE	2253	145	49	0	0	0	40.5
20b	1.2	n	EE	2250	138	49	0	0	0	40.5
20c	1.2	n	EE	2248	136	47	0	0	0	40.5

Note. Complete list of all cluster simulations run for this study. In column 2, we list the initial r_i for each simulation. In column 3, we indicate whether or not primordial mass segregation is assumed. In column 4, we indicate the assumed prescription for giant collisions, where “SS” indicates the sticky sphere approximation and “EE” indicates the envelope ejection prescription, as described in the text. Column 5 shows the total number of BHs retained at birth in each simulation. Column 6 shows the number of these BHs that underwent at least one stellar collision prior to formation. Columns 7, 8, 9, and 10 show the total number of PPSNe, PISNe, mass-gap BHs, and IMBHs in each simulation, respectively. The final column (11) shows the mass of the most massive BH formed in each simulation.

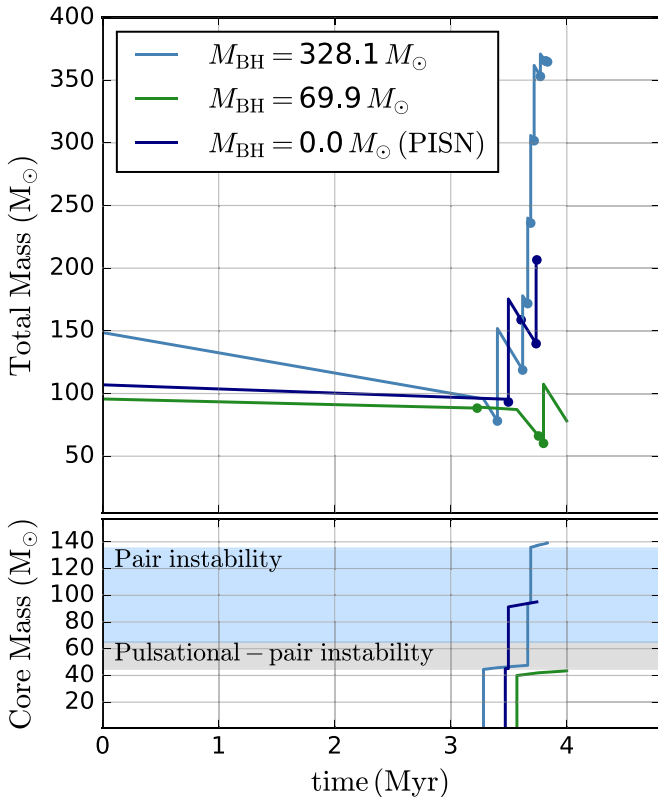


Figure 2. Total mass (top panel) and core mass (bottom panel) vs. time for three collision outcomes in simulation 2c. The filled circles in the top panel indicate collision events. The detailed collision histories for each of these three outcomes are shown in Figure 3 and also listed in Tables 4–6 in the Appendix.

In Figure 4, we show the BH mass versus initial mass for each BH formed in our simulations. For BHs formed through stellar evolution alone (i.e., they never undergo a collisions prior to core collapse), the initial mass corresponds to the zero-age

main-sequence (ZAMS) mass. In this case, the $M_{\text{BH}} - M_{\text{ZAMS}}$ relation is well-defined and is shown by the solid black curves. For $M_{\text{ZAMS}} \lesssim 40 M_{\odot}$, M_{BH} is determined by the assumed fallback prescription (here we assume the “delayed” model from Fryer et al. 2012), for M_{ZAMS} in the range $\approx 40\text{--}100 M_{\odot}$, M_{BH} is determined primarily by the assumed wind-mass-loss model, and for $M_{\text{ZAMS}} \gtrsim 100 M_{\odot}$, M_{BH} is determined primarily by the assumed pair instability physics.

In blue, we show those BHs that formed through stellar collisions. For these objects, we simply define the initial mass as the ZAMS mass of the more massive of the two collision components at the moment of the first collision in the BH’s history. The horizontal gray bands in each panel illustrate the pair-instability mass gap.

In Table 2, we compare BH formation efficiencies (the number of BHs formed per unit stellar mass) for the four different physics prescriptions adopted in our simulations. In columns 3 and 4, we show efficiencies for BHs in the pair-instability gap and IMBHs, respectively. In columns 5 and 6, we show the fraction of the total mass that forms pair-instability BHs and IMBHs, respectively. In the bottom row of Table 2, we show for comparison the formation efficiencies computed from the simulations described in Di Carlo et al. (2019) and Di Carlo et al. (2020). We discuss comparisons with these earlier analyses in detail in Section 6.2.

As Figure 4 and Table 2 show, BHs with masses within or above the pair-instability mass gap form most readily in the simulations with primordial mass segregation and which treat giant collisions in the sticky sphere approximation. This is as anticipated: primordial mass segregation leads to more massive star collisions and the sticky sphere approximation leads to more significant mass growth during the collisions.

As the lower two panels of Figure 4 show, we find that the envelope ejection prescription for giant collisions leads to a population of BHs with masses lower than those predicted from single star evolution. In this limit, if a giant star (en route to stellar core collapse and BH formation) collides with another

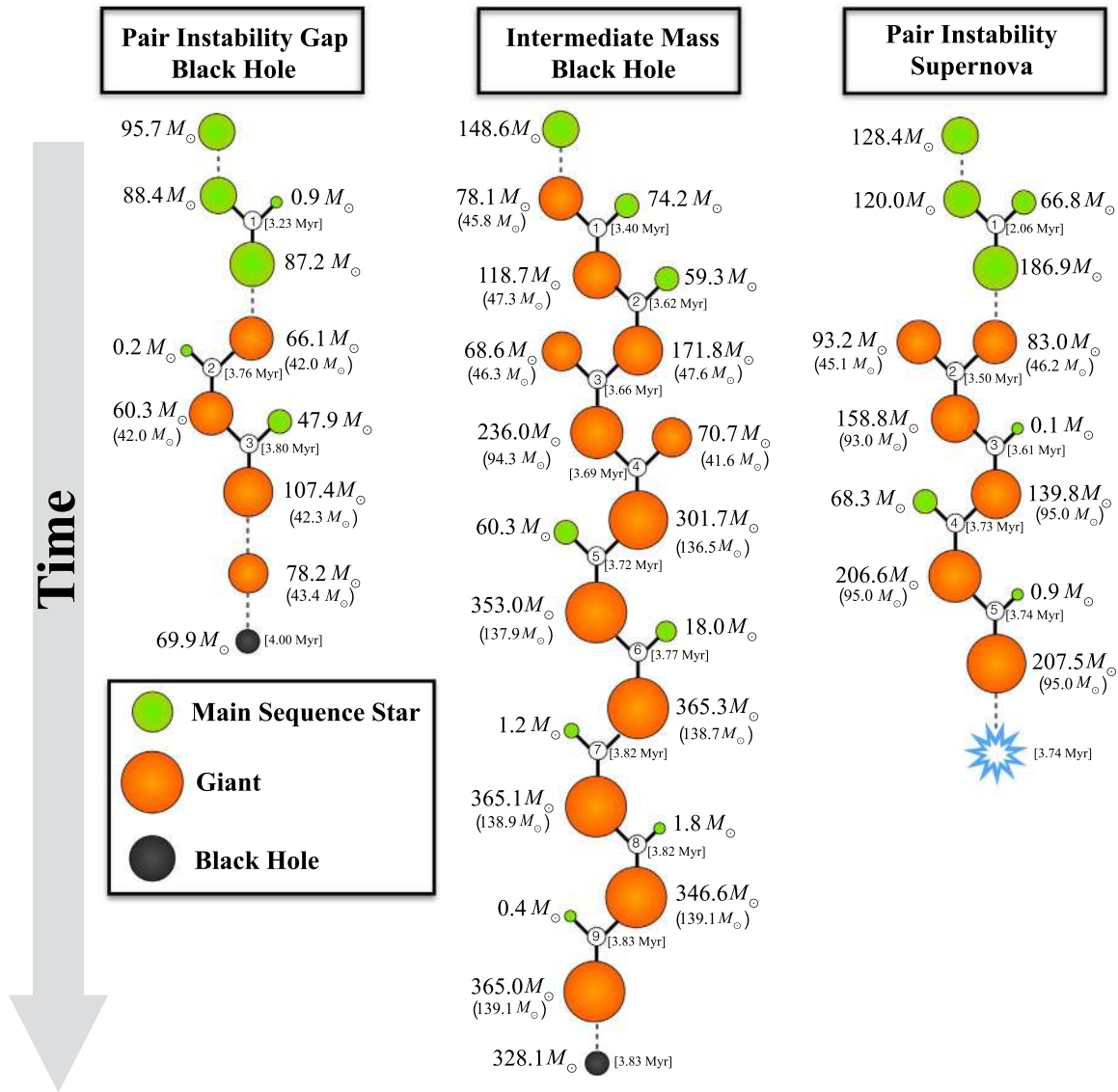


Figure 3. Example collision histories for the three distinct massive star collision outcomes described in the text. We show the total mass of each object next to each collision component and product. We show in parentheses the core mass of each object and in brackets the time of each collision. The pair instability gap BH, IMBHs, and PISNe histories corresponds to the green, light blue, and navy curves, respectively, in Figure 2.

star and loses its envelope, core growth may be inhibited such that at the time of core collapse, the core mass is lower than if the star had evolved uninterrupted. In this case, a lower-mass BH results in a process we label as an “inverse runaway.” This effect is most pronounced if the giant collides with a low-mass main-sequence star, in which case the new giant formed through the collision has an envelope significantly less massive than its pre-collision progenitor. As pointed out in Kremer et al. (2020), for a non-mass-segregated cluster where stars of all masses are equally mixed, massive stars are most likely to undergo collisions with low-mass MS stars, simply because these stars dominate the assumed IMF. However, for a mass-segregated cluster where stars tend to interact with other stars of similar total mass (see Figure 1), collisions with mass ratios near unity are more common. Thus, in a primordially segregated cluster, giants typically collide with MS stars that are more massive compared to those in nonsegregated clusters. As a result, MS–giant collisions preferentially create collision products with a higher envelope mass (therefore yielding more

massive BHs) in initially segregated clusters compared to clusters that are not primordially segregated (which produce lower-mass BHs; compare the bottom-left and bottom-right panels in Figure 4). Note that even in the “envelope ejection” limit, a population of overmassive BHs may still form through the standard runaway process, depending upon the collision histories. Indeed, in the bottom two panels of Figure 4, two distinct BH populations are visible, particularly notable for initial masses in the range 20–40 M_{\odot} . Here, the location of a given BH in the overmassive versus the undermassive population is determined by its specific collision history.

4. Implications for GW Astrophysics

If the BHs within or above the pair-instability mass gap go on to merge with one another or with other lower-mass BHs through dynamical interactions, these mergers have important implications to GW science. In particular, if such mass-gap mergers are detected by instruments such as LIGO/Virgo, it

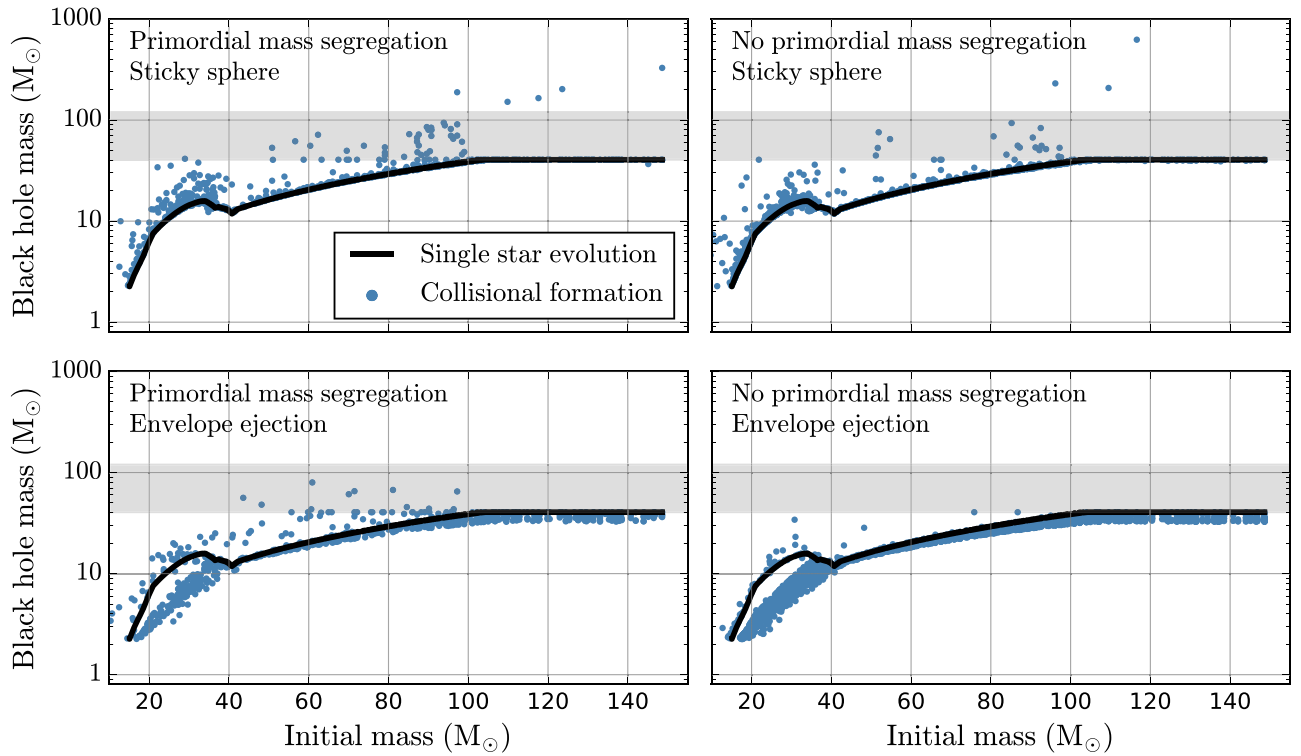


Figure 4. BH mass vs. initial mass for all BHs formed through stellar collisions (blue points) in the four groups of models. The black curves show the $M_{\text{BH}} - M_{\text{ZAMS}}$ tracks for single star evolution and the shaded gray regions indicate the mass gap expected from PISNe. The top-left (top-right) panel shows models that assume primordial mass segregation (no primordial mass segregation) and sticky sphere limit for giant collisions. The bottom-left (bottom-right) panel shows models that assume primordial mass segregation (no primordial mass segregation) and the envelope ejection limit for giant collisions.

Table 2
BH Formation Efficiency for Different Prescriptions

Prim. MS	Giant coll.	N_{PI}/M_{\odot}	$N_{\text{IMBH}}/M_{\odot}$	M_{PI}/M_{\odot}	$M_{\text{IMBH}}/M_{\odot}$
y	SS	4.2×10^{-6}	5.3×10^{-7}	2.5×10^{-4}	1.1×10^{-4}
n	SS	2.0×10^{-6}	3.4×10^{-7}	1.2×10^{-4}	1.2×10^{-4}
y	EE	2.8×10^{-6}	0	1.7×10^{-4}	0
n	EE	0	0	0	0
Di Carlo et al. (2020)		4.2×10^{-5}	2.4×10^{-6}	3.4×10^{-3}	5.5×10^{-4}

Note. In rows 1–4 we list the BH formation efficiency for the various prescriptions adopted in this study. In row 5 we list for comparison the formation efficiency from the lower-mass cluster simulations computed in Di Carlo et al. (2020). In rows 3 and 4 we list the total number of pair-instability gap BHs (N_{PI}) and IMBHs (N_{IMBH}) per unit stellar mass, respectively, and in rows 5 and 6 we list the total mass of pair-instability gap BHs and IMBHs per unit stellar mass, respectively.

would provide constraints on the contribution of dynamical environments to the overall BBH merger rate. Indeed, the probability that at least one of the components of the recently detected event GW190521 (inferred component masses of $85^{+21}_{-14} M_{\odot}$ and $66^{+17}_{-18} M_{\odot}$) falls within the pair-instability mass gap is 99% (Abbott et al. 2020a, 2020b).

In order to investigate this topic, we run seven of the simulations show in Table 1 for 12 Gyr, recording all BBH mergers that occur. For these simulations, we adopt exclusively the sticky sphere assumption for giant collisions, as this approximation was shown in Section 3 to yield the highest formation rate of mass-gap BHs. In this case, one could regard

the results of this section as an upper limit on the true number of collisional mass-gap mergers.¹⁷

In Figure 5, we show the mass distribution for all BHs that undergo BBH mergers in these seven simulations. The black histogram shows those merging BHs that form through single star evolution, the blue histogram shows the BHs that form through collisions of young massive stars (as in Section 3), and the green histogram shows the second-generation BHs that are formed through earlier BBH mergers. The gray background illustrates the pair-instability mass gap.

Of the 259 total BBH mergers occurring in this set of simulations, 95 (37%) feature at least one component that underwent at least one stellar collision before BH formation. If the stellar collision process encodes itself upon the BH that ultimately forms (for example, by altering the BH’s mass, as discussed next, or spin, as discussed briefly in Section 6), this may yield an observable fingerprint upon potential GW detections.

In total, 16 of the 259 total BBH mergers (6%) involve at least one component with a mass in the pair-instability gap. Of these 16 mass-gap mergers, seven (3% of the 259 total) feature at least one BH formed through stellar collisions, and 11 (4% of the 259 total) feature at least one second-generation BH. Thus, the stellar-collision channel may rival the multiple-generation channel as a mechanism for producing mass-gap BBH mergers. We do note that Rodriguez et al. (2019) identified a larger fraction of second-generation mergers (roughly 10% of all BBH mergers) compared to the 4% identified here. This is not

¹⁷ Again noting the caveat that we assume here zero primordial binaries. Higher binary fractions may increase both the number of pair-instability gap BHs (Di Carlo et al. 2019, 2020; see also Section 6) and also the number of BBH mergers (e.g., Chatterjee et al. 2017b).

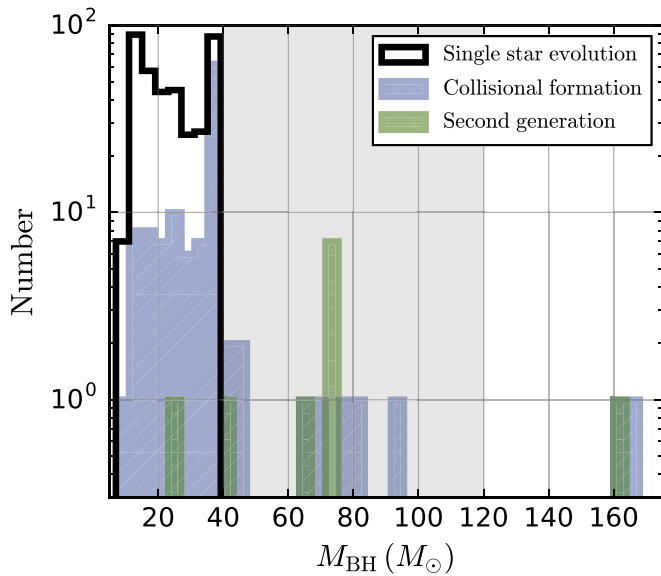


Figure 5. Mass distribution for all BHs that undergo mergers in the seven simulations evolved for 12 Gyr. The black histogram shows the merging BHs that form through single star evolution, the blue histogram shows those that form through collisions (see Section 3), and the green histogram shows the second-generation BHs that formed through earlier BBH mergers. The shaded gray region indicates the mass gap expected from PPSNe and PISNe for single star evolution.

surprising given that Rodriguez et al. (2019) examined more massive clusters models (up to $\sim 10^6 M_\odot$ at birth, over twice as massive as the models considered in this study). Due to their higher escape velocities, more massive clusters retain a larger fraction second-generation BHs upon formation. We can speculate that more massive (and therefore more dense) clusters will also yield a larger number of massive star collisions, and therefore more collisional mass-gap BHs, but more detailed models are necessary to test this. We discuss this topic further in Section 6.

In Table 3, we list the properties of these 16 mass-gap mergers, including merger time (relative to the host cluster birth time), component masses, and merger channel. In this table, BH masses marked with a \star are formed through stellar collisions, while those marked with a \dagger are formed through BBH mergers. In column 5, we show the channel through which each listed BBH merger occurs. Here “binary” mergers are in-cluster mergers occurring through two-body GW inspiral, “binary–single” and “binary–binary” mergers are in-cluster mergers that occur through close passages during 3- and 4-body resonant encounters, and “ejected” mergers are those that are dynamically ejected from their host clusters and merge as isolated binaries. See Samsing & D’Orazio (2018), D’Orazio & Samsing (2018), Rodriguez et al. (2018a), Zevin et al. (2018), and Kremer et al. (2020) for a summary of the different BBH merger channels in dense star clusters.

In column 6 in Table 3, we note whether each merger is ejected or retained post-merger (determined by the relative value of the computed GW recoil kick and current cluster escape velocity). Mergers marked “N/A” were ejected from their host cluster prior to merger. Of the seven BBH mergers listed that occur in their host cluster, all but one are ejected post-merger through GW recoil. Indeed, the one mass-gap merger product that is retained (the $94 M_\odot + 80 M_\odot$ merger where both components are formed through stellar collisions) is ejected from the cluster shortly thereafter through a binary–

Table 3

All Binary BH Mergers with at Least One Component in the Upper-mass Gap

Model	t_{merge} (Gyr)	M_1	M_2	Type	Outcome
2a	0.06	94.2 \star	80.1 \star	Binary	Retained
2a	0.15	71.6 \star	77.1 \dagger	Binary–binary	Ejected
2a	0.21	36.4	47.6 \star	Binary–single	Ejected
2a	1.37	25.4	53.3 \dagger	Binary	Ejected
2a	1.7	40.5	165.9 \star, \dagger	Ejected	N/A
2b	0.71	40.5	168.0 \star	Ejected	N/A
3a	0.15	66.1 \star	76.2 \dagger	Binary	Ejected
3a	0.21	33.3	77.1 \dagger	Binary	Ejected
3a	12.92	33.9	73.8 \dagger	Ejected	N/A
4a	0.55	40.5	77.1 \dagger	Ejected	N/A
5a	0.46	38.1	45.4 \star	Ejected	N/A
5a	7.77	33.9	76.8 \dagger	Ejected	N/A
5b	0.68	33.9	74.2 \dagger	Binary–binary	Ejected
5b	9.8	40.5	85.0 \star	Ejected	N/A
6a	0.29	40.5	73.9 \dagger	Ejected	N/A
6a	11.61	36.3	41.5 \dagger	Ejected	N/A

Note. List of all BBH mergers in the seven simulations integrated to 12 Gyr with at least one component in the pair-instability mass gap. BH masses with marked with a \star are formed through stellar collisions and BH masses marked with a \dagger are second-generation BHs formed through previous BBH mergers. The 165.9 M_\odot object marked with both symbols was formed through the merger of a pair of BHs one of which was itself formed through collisions. The fifth column notes the merger channel for each binary (see text for details) and the sixth column denotes the merger outcome (if the merger product is retained post-merger or is ejected due to the GW recoil kick).

binary resonant encounter. Thus, as has been shown through various other analyses (e.g., Antonini & Gieles 2020), GW recoil kicks combined with the relatively low escape velocities of typical GCs prevents the buildup of massive BHs (i.e., IMBHs) through repeated BH mergers. As discussed in Section 3, runaway stellar mergers are a far more viable channel for producing IMBHs beyond with masses far in excess of the pair-instability mass gap.

Previous analyses (e.g., Gnedin et al. 2014; Ziosi et al. 2014; Banerjee 2018; Fragione & Kocsis 2018; Rodriguez & Loeb 2018; Di Carlo et al. 2019; Kremer et al. 2020) have predicted the overall BBH merger rate from clusters to be as high as $20 \text{ Gpc}^{-3} \text{ yr}^{-1}$ in the local universe, within the uncertainty bounds of the merger rates inferred from the LIGO/Virgo O2 catalog, $53.2^{+58.5}_{-28.8} \text{ Gpc}^{-3} \text{ yr}^{-1}$ (The LIGO Scientific Collaboration et al. 2019b, 2019a). We find that up to roughly 37% of all BBH mergers in clusters may host at least one BH formed through stellar collisions and that up to roughly 3% of all mergers include at least one mass-gap BH that formed through stellar collisions. From these numbers, we can infer a rough estimate of the rate of mass-gap mergers of $0.6 \text{ Gpc}^{-3} \text{ yr}^{-1}$ from stellar collisions in clusters. We note this is consistent with the $\approx 0.1 \text{ Gpc}^{-3} \text{ yr}^{-1}$ rate inferred by LIGO/Virgo for GW190521-like events, but caution that more detailed analysis is necessary to make precise comparisons and rate predictions. Regardless, we can conclude that the overall rate of collisional BH mergers may constitute an observable fraction of GW events detected by LIGO/Virgo.

5. PISNe and Other Electromagnetic Transients

In this section, we compute rates (Section 5.1) and discuss observational prospects (Section 5.2) for PISNe and a number of other possible electromagnetic transients associated with the outcomes of stellar collisions seen in our simulations. Because we identify PISNe only in those simulations adopting the sticky sphere limit for giant collisions, we consider only these simulations in this section (simulations 2–10 in Table 1; neglecting simulations 1a–c that undergo collisional run-aways). In this case, the rate predictions presented in this section may be regarded as upper limits.

5.1. Rates

In order to estimate the cosmological rates of various SN events, we adopt a method similar to that implemented in Kremer et al. (2020) to compute BBH merger rates. Here the cumulative rate is given by

$$R(z) = \int_0^z \mathcal{R}(z') \frac{dV_c}{dz'} (1+z')^{-1} dz', \quad (2)$$

where dV_c/dz is the comoving volume at redshift z and $\mathcal{R}(z)$ is the comoving (source) rate given by $\mathcal{R}(z) = \rho_{GC} \times \frac{dN(z)}{dt}$, where ρ_{GC} is the volumetric number density of clusters, assuming a constant value of $\rho_{GC} = 2.31 \text{ Mpc}^{-3}$ (consistent with Rodriguez et al. 2015; Rodriguez & Loeb 2018; Kremer et al. 2020) and $dN(z)/dt$ is the number of events per unit time at a given redshift.

We compute $dN(z)/dt$ using a procedure similar to that of Kremer et al. (2020): first, we generate a complete list of event times (t_{SN}) for all SNe occurring in our model set. For each of these events, we draw 200 random ages (t_{age}) for the host cluster in which the SN occurred. We then compute the effective event time for each SN as $t_{effective} = t_{Hubble} - t_{age} + t_{SN}$. We draw cluster ages from the age distributions of El-Badry et al. (2019).¹⁸ We then compute the number of events per time, $dN(z)/dt$, by dividing this list of effective event times into separate redshift bins, accounting for the oversampling of age draws and total number of simulations (35 total that adopt the sticky sphere limit; see Table 1).

The cluster simulations in this analysis have initial masses of roughly $4 \times 10^5 M_\odot$ and present day (i.e., at $t \approx 12 \text{ Gyr}$) of roughly $2 \times 10^5 M_\odot$,¹⁹ matching well the median cluster mass observed for the Milky Way GCs (e.g., Harris 1996; Baumgardt & Hilker 2018; Kremer et al. 2020). However, as described in Rodriguez et al. (2015) and Kremer et al. (2020) in the case of BBH mergers, adopting this simulation mass as our typical cluster causes an underestimation of the total rate, because it does not properly account for the contribution of the cluster mass function’s high-mass tail not covered by our models, which as shown in Kremer et al. (2020) may yield a rate higher by a factor of a few. A careful examination of the way the total number of PISNe and other SN events per model scales with N is beyond the scope of this paper. We simply note

¹⁸ Note that cluster age distributions are metallicity-dependent (see El-Badry et al. 2019), however, the simulations of this study adopt a fixed metallicity. For simplicity, we ignore metallicity effects for the rate calculation, and refer the reader to Di Carlo et al. (2020) for a discussion of the effect of metallicity in regards to stellar collision outcomes in dense clusters.

¹⁹ The cluster mass loss is governed by both stellar wind-mass loss and dynamical ejection of stars throughout the cluster’s lifetime.

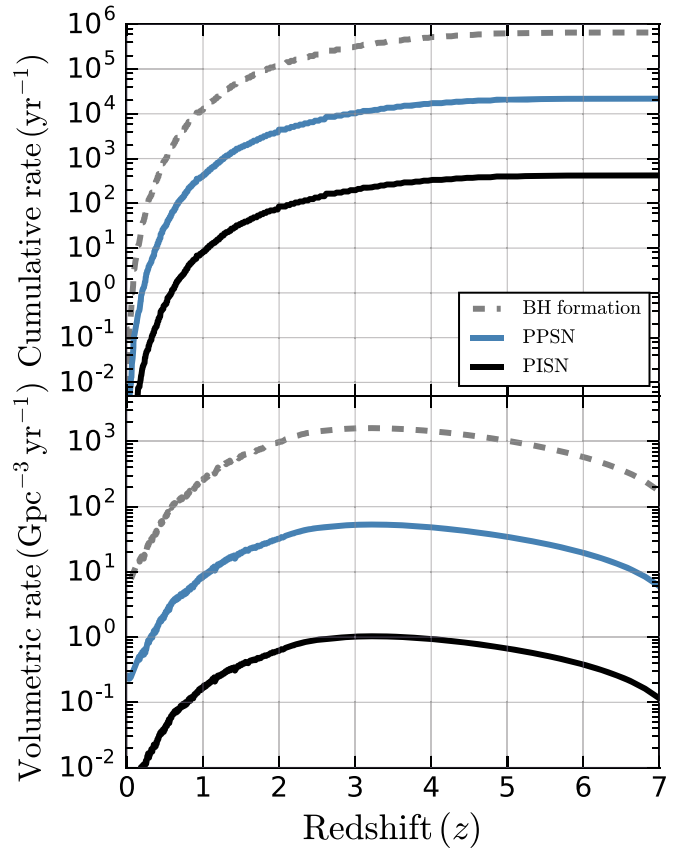


Figure 6. Cumulative (top panel) and volumetric (bottom panel) rates for various classes of SNe as computed from our simulations.

that the rates presented here may in factor underestimate the true rate of these events.

We show in Figure 6 the results of these rate calculations for PISNe (black curve) and for PPSNe (blue curve). We also show (dashed gray curve) the formation rate of all BHs, which may be associated with standard core-collapse SNe. Note that because BH formation occurs exclusively at early times ($t \approx 3\text{--}20 \text{ Myr}$), the shape of these curves are roughly identical and are determined primarily by the assumed cluster birth time distribution.

5.2. Observational Prospects

As described in Section 2, PISNe are thought to occur for stars with helium core masses in the range $\approx 65\text{--}135 M_\odot$. At zero metallicity (i.e., Population III stars), this corresponds to ZAMS masses in the range $\sim 140\text{--}260 M_\odot$ (e.g., Spera & Mapelli 2017). At higher metallicities where line-driven stellar winds (e.g., Vink et al. 2001) are expected to drive efficient mass loss, even larger ZAMS masses are likely required to produce helium cores within the range required for a PISN. However, myriad observations suggest an upper limit to the stellar IMF for Population I/II stars of roughly $150 M_\odot$ (e.g., Kroupa 2001; Figer 2005; Weidner et al. 2010; Bastian et al. 2010). This may suggest that PISNe are prevented for Population I/II stars and thus prevented at redshifts $z \lesssim 6$, which corresponds roughly to the end of the reionization epoch at which the universe become sufficiently metal-enriched to prohibit Population III star formation (e.g., Bromm & Loeb 2003).

From an observational perspective, PISNe are expected to be characterized by very bright (as high as $\sim 10^{44} \text{ erg s}^{-1}$) and broad light curves (rise times as long as $\sim 150 \text{ days}$) as a

consequence of the large ejecta masses, and therefore, long diffusion times (e.g., Dessart et al. 2013; Kozyreva et al. 2014). A number of observed events have been associated with PISNe, including SN 2006gy (Smith et al. 2007), SN2007bi (Gal-Yam et al. 2009), SN 2213-1745 (Cooke et al. 2012), OGLE14-073 (Terreran et al. 2017), SN 2016iet (Gomez et al. 2019), and SN2016aps (Nicholl et al. 2020). Several of these candidates have been observed at low redshift, implying that potential formation pathways for PISNe do indeed exist for higher-metallicity Population I/II stars.

As demonstrated here and in other earlier analyses (e.g., Langer et al. 2007; Portegies Zwart & van den Heuvel 2007; Yungelson et al. 2008; Glebbeek et al. 2009; Pan et al. 2012) the formation of massive stars through stellar collisions in dense star clusters may provide a viable pathway to PISNe. In total, we predict a volumetric rate of roughly $0.1 \text{ Gpc}^{-3} \text{ yr}^{-1}$ in the local universe ($z < 1$), roughly consistent with the rate predicted in Pan et al. (2012), which adopted a simple analytic rate estimate using theoretical estimates of cluster and stellar properties. We reserve a more detailed examination of the electromagnetic signatures (e.g., light curves) of the PISNe (as well as PPSNe and other SN types) identified in our simulations for a later study. We do note however, that Pan et al. (2012) estimated, using simulated PISN light curves from Kasen et al. (2011), that the Large Synoptic Survey Telescope (LSST) may observe ~ 100 PISNe per year that originated from collisional runaways in young massive clusters. Thus, in the coming years LSST may indeed place further constraints upon the processes discussed here.

6. Discussion and Conclusions

6.1. Summary

We have explored ways in which stellar collisions (or series of stellar collisions) in dense star clusters may lead to several unique evolutionary outcomes not possible for single star evolution. In particular, we have examined the role played by stellar collisions in navigating the gap expected in the BH mass function caused by the pair instability and pulsational pair instability. By computing a large set of independent cluster simulations with cluster masses ($M = 4 \times 10^5 M_{\odot}$) comparable to the GCs observed in the Milky Way, we have demonstrated the dynamical formation of (1) BHs with masses occupying the mass gap expected due to PPSNe and PISNe, (2) massive stars that undergo PISNe, and (3) massive stars with helium cores beyond the boundary where the pair instability is expected to operate which directly collapse into IMBHs with masses in excess of $\sim 100 M_{\odot}$.

We explored also the dependence of these three outcomes upon two theoretical uncertainties: the degree of primordial mass segregation in the host clusters and the efficiency of envelope ejection during giant star collisions. Together, these two theoretical uncertainties roughly bracket the range of expected outcomes. On the one extreme (assuming complete primordial mass segregation and full sticky sphere collisions), massive BHs readily form through successive stellar collisions. On the other hand (assuming no primordial mass segregation and that giant envelopes are ejected), we observe “inverse runaways” where successive collisions can lead to stripping which ultimately may produce lower-mass BHs.

We showed that the population of BHs with masses in or above the pair-instability gap go on to form binaries and merge

with other BHs, creating a unique class of upper-mass-gap BBH mergers that may be detectable as GW sources by LIGO/Virgo, similar to the recent event GW190521. We showed in particular that the collisional formation scenario studied here may compete with the previously explored multiple-generation-merger channel for producing BHs in the pair-instability gap.

Finally, we computed the volumetric merger rate of a number of SN classes originating in massive star clusters, most notably PISNe, which result uniquely from stellar collisions. A number of observed transients have been speculatively linked with PISNe. In the coming years, LSST may provide further constraints upon the potential role of stellar clusters in producing PISNe and other transients.

6.2. Comparison with Previous Results

Prior to our present work in the massive star-cluster regime, Di Carlo et al. (2019) and Di Carlo et al. (2020) explored the formation of massive BHs in relatively low-mass young star clusters. In this section, we compare our results to those of these previous studies. Such comparisons provide a critical test of our results, help determine the role of differing physical prescriptions across multiple cluster dynamics codes, and, ultimately, constrain ways massive BH formation efficiency varies across the cluster mass function.

Di Carlo et al. (2019) and Di Carlo et al. (2020) computed a set of 5×10^3 direct N -body simulations of young star clusters with metallicity $Z = 0.002$ and initial masses ranging from $10^3 M_{\odot}$ to $3 \times 10^4 M_{\odot}$. These simulations were performed using the code NBODY6++GPU (Wang et al. 2015), coupled with the population synthesis code MOBSE (Giacobbo et al. 2018). There are several differences between MOBSE and the BSE stellar-evolution prescriptions implemented in CMC that are relevant for stellar collisions and massive BH formation. First, the rejuvenation factor f_{rejuv} is set equal to 0.1 in MOBSE, meaning that the collision products are more rejuvenated than in CMC. The mass of the collision product in MOBSE is obtained as in the sticky sphere prescriptions in CMC, with the exception that if two main-sequence stars collide, the mass of the collision product is $M_3 = M_1 + 0.7M_2$. Additionally, MOBSE uses the fitting formulae provided by Spera & Mapelli (2017) to determine the remnant mass after a PPSN. The implementation of such formulae in MOBSE is described in the appendix of Giacobbo et al. (2018). As a result, the MOBSE pair-instability gap for BHs occupies the range $60\text{--}150 M_{\odot}$, compared to CMC where the assumed range is $40.5\text{--}120 M_{\odot}$.

As shown in Table 2, the efficiencies of the Di Carlo et al. (2020) analyses are roughly a factor of 10 larger than those predicted from the CMC simulations. There are two primary reasons for this result. First, unlike the CMC simulations, which assume zero primordial binaries, the Di Carlo et al. (2020) simulations adopt a primordial binary fraction $f_{\text{bin}} = 0.4$. As shown in a number of previous analyses (e.g., Fregeau & Rasio 2007), higher binary fractions lead to a higher rate of stellar collisions simply because binaries have a larger cross section for interaction. Second, the Di Carlo et al. (2020) simulations adopt fractal initial conditions in order to mimic the clumpy and asymmetric structure observed in star-forming regions (e.g., Cartwright & Whitworth 2004; Gutermuth et al. 2005). Coupled with their assumed initial half-mass radii (derived from the Marks & Kroupa relation; Marks et al. 2012), these fractal clumps produce regions with density

$\rho > 10^6 M_{\odot} \text{pc}^{-3}$. As shown in Figure 1, this is higher than the densities of our CMC simulations in all but the innermost cluster regions. These overdense fractal regions combined with the higher binary fractions lead to an increased rate in stellar collisions in the Di Carlo et al. (2020) simulations, thus leading to a higher formation efficiency of both mass-gap BHs and IMBHs.

Using the results of Section 3 and normalizing by total simulated mass, we find an overall BBH merger efficiency (i.e., number of mergers per stellar mass) of $8 \times 10^{-5} M_{\odot}^{-1}$ for the CMC simulations. For mergers in which at least one component is a pair-instability gap BH formed through collisions (multiple BH mergers), the merger efficiency is $2 \times 10^{-6} M_{\odot}^{-1}$ ($3 \times 10^{-5} M_{\odot}^{-1}$). In contrast, the overall BBH merger efficiency from the Di Carlo et al. (2020) simulations is $1.3 \times 10^{-5} M_{\odot}^{-1}$, while the merger efficiency with at least one component in the pair-instability gap is $2.5 \times 10^{-7} M_{\odot}^{-1}$. Thus, although the Di Carlo et al. (2020) simulations are more efficient (by a factor of ~ 10) in producing pair-instability gap BHs, they are less efficient (by a factor of ~ 10) in producing pair-instability gap mergers. This is anticipated. In the Di Carlo et al. (2020) simulations (which have lower N compared to the CMC models), a significant amount of the available mass of high-mass stars must be utilized to create a single massive BH. Thus, in the case that a massive BH is formed, the number of available companions in the host cluster is fewer. However, in the CMC simulations, there are many available companions both because N is larger and because the escape velocity is larger, allowing the cluster to retain a larger fraction of lower-mass BHs that may be kicked out of lower-mass clusters through natal kicks.

As can be read from the fifth column of Table 3, seven of the 16 total mass-gap mergers seen in the CMC simulations occur within their host cluster. This in contrast to the Di Carlo et al. (2020) simulations where *all* BBH mergers occur after ejection from their host cluster (including also most of the low-mass mergers where both components lie below the pair-instability gap). This is simply because the low-mass Di Carlo et al. (2020) simulations have lower escape velocities. As a consequence, the Di Carlo et al. (2020) simulations produce no second-generation BHs. This is a key difference between low-mass clusters and the higher-mass clusters considered in this study.

Ultimately, a more complete study implementing self-consistent binary evolution, stellar collision prescriptions, and cluster initial conditions is needed to determine more precisely the differences between the low-mass simulations of Di Carlo et al. (2019, 2020) and the high-mass clusters of the present study.

6.3. Future Work

A number of elements have been left unexplored in detail in this analysis. Here, we briefly summarize a few such points and describe several avenues for future study.

We have assumed a fixed metallicity of $Z = 0.002 = 0.1 Z_{\odot}$ for all simulations computed in this study. Previous studies (e.g., Glebbeek et al. 2009; Di Carlo et al. 2020) have shown that metallicity can have a significant effect upon growth through stellar collisions, and therefore upon the mass of the BH ultimately formed. Specifically, both of the aforementioned analyses showed that at higher metallicities (especially approaching Z_{\odot}) mass growth can be significantly limited. In the context of low-mass clusters, Di Carlo et al. (2020) showed

in particular that at solar metallicity, roughly an order-of-magnitude fewer pair-instability gap BHs form compared to simulations with $0.1 Z_{\odot}$. This is driven primarily by the assumed metallicity-dependent wind-mass-loss prescriptions (Vink et al. 2001). Furthermore, aside from metallicity dependencies, stellar winds may operate very differently for massive stars ($M \gtrsim 150 M_{\odot}$) compared to lower-mass stars. An alternative treatment of massive star winds may have a substantial effect on the evolution of collision products, particularly for collisions of main-sequence stars (e.g., Glebbeek et al. 2009; Chatterjee et al. 2009). We reserve a more detailed examination of the effects of stellar winds on massive BH formation for future studies.

In the simulations computed in this study, we assume for simplicity that BHs are born with zero natal spin (dimensionless spin parameter $a = 0$). This is in part motivated by recent work (Fuller & Ma 2019) suggesting that stellar-mass BHs are born with low spins, however, other work (for example, the analysis of the spins of BHs found in high-mass X-ray binaries; Miller & Miller 2015; Fragos & McClintock 2015) suggest some BHs may in fact be born with high spins. In reality, the true values of BH spins remain highly uncertain (e.g., Heger et al. 2005; Lovegrove & Woosley 2013; Qin et al. 2019). However, it is understood that the GW recoil of a BBH merger product is highly sensitive to the spins (both spin magnitude and relative orientation) of the merger components (e.g., Merritt et al. 2004; Campanelli et al. 2007; Berti et al. 2007; Lousto et al. 2012; Gerosa & Berti 2019). In general, as spin magnitudes increase, the recoil velocity increases. For in-cluster BBH mergers, this means that rapidly spinning BHs are more likely to be ejected from their host cluster upon merger, thus inhibiting the rate of second (and higher) generation mergers. Indeed, Rodriguez et al. (2019) showed that even for dimensionless spin parameters of $a = 0.2$, the rate of second-generation BBH mergers with at least one component in the pair-instability gap nearly vanishes. Thus, if in fact some (or all BHs) are born with nonzero spins, the stellar-collision channel may in fact dominate over the second-generation merger channel in terms of the overall rate of mass-gap BBH mergers from dense clusters.

On this note, we have shown that roughly 37% of all BBH mergers feature at least one BH component that was formed through stellar collisions. Although highly uncertain, we can speculate that these collisions may lead to stellar spin-up (if the collision is off-center, some fraction of the orbital angular momentum of the pair of stars may be transferred to spin angular momentum of the collision product). This may affect the spin of the BH when the collision product ultimately undergoes core collapse. Along these lines, Batta & Ramirez-Ruiz (2019) explored the masses and spins of BH remnants formed through the collapse of rotating, helium star pre-SN progenitors and showed that progenitor stars with rotation rates large enough to form an accretion disk may unbind their outer layers through accretion feedback and produce BHs with only a fraction of the total mass of their progenitors. Furthermore, Gaburov et al. (2010) showed that mass loss during stellar collisions may result in stellar kicks of $\sim 10 \text{ km s}^{-1}$. Such kicks, which have not been considered here, may affect the long-term dynamics of the collision products and may be particularly important in lower-mass clusters with lower escape speeds. Ultimately, all these speculations should be tested with more detailed hydrodynamic models capable of computing spin

angular momenta of collision products (e.g., Lombardi et al. 2002) coupled with more detailed stellar evolution models (e.g., MESA; Paxton et al. 2015).

For most of the cluster simulations considered in this study, we identify only one to four BHs in the pair-instability gap with large variations in the maximum BH mass, even between multiple realizations of the same initial conditions. The present study aims to simply demonstrate that the formation of pair-instability gap BHs and IMBHs through stellar collisions is, in principle, possible in GCs. Given the small number statistics at play, a more expansive set of models, with a large number of independent realizations per set of initial conditions, may be necessary to pin down more precisely the typical masses and numbers massive BHs.

We have assumed here a standard IMF from Kroupa (2001) for all models, consistent with a large body of previous cluster modeling work. However, some recent analyses suggest that a top-heavy IMF may be appropriate in some contexts (e.g., Marks et al. 2012; Schneider et al. 2018). A top-heavy IMF will lead to increased rate of massive star collisions and thus may lead to an increased rate of massive BH formation (both pair-instability gap BHs and IMBHs). We reserve detailed exploration of the effect of IMF variations for future work.

Finally, in several of the simulations computed in this study, we demonstrated the formation of very massive stars in excess of $1000 M_{\odot}$ that may ultimately directly collapse into IMBHs of comparable mass. IMBHs have long been a hotly debated topic due to their potential role in not only GC dynamics (e.g., Greene et al. 2019) but also in cosmology and galaxy formation, as they could be the seeds for the supermassive BHs observed at the centers of most galaxies (e.g., Katz et al. 2015). In spite of the inherent interest in these objects, observational evidence for the presence of an IMBH in any GC, either from X-ray and radio observations (e.g., Tremou et al. 2018) or from dynamical measurements (e.g., Noyola et al. 2010; Lützgendorf et al. 2011; Feldmeier et al. 2013; Perera et al. 2017) remains controversial (e.g., Gieles et al. 2018; Zocchi et al. 2019). Nonetheless, the role that IMBHs, if present, may play in the production of GW sources (e.g., Amaro-Seoane et al. 2007; Mandel et al. 2008;

MacLeod et al. 2016; Fragione et al. 2018a, 2020; María Ezquiaga & Holz 2020), high-energy transients such as tidal disruption events (e.g., Rosswog et al. 2009; MacLeod et al. 2014, 2016; Fragione et al. 2018b), and GC dynamics more broadly is a rich topic that we hope to explore in more detail within the scope of CMC in a later study.

This work was supported in part by NSF Grant AST-1716762 at Northwestern University. K.K. is supported by an NSF Astronomy and Astrophysics Postdoctoral Fellowship under award AST-2001751. M.S. acknowledges funding from the European Union’s Horizon 2020 research and innovation program under the Marie-Skłodowska-Curie grant agreement No. 794393. S.C. acknowledges support of the Department of Atomic Energy, Government of India, under project no. 12-R&D-TFR-5.02-0200. G.F. acknowledges support from a CIERA Fellowship at Northwestern University. C.R. was supported by an ITC Postdoctoral Fellowship from Harvard University. This work used computing resources at CIERA funded by NSF PHY-1726951.

Software: CMC (Joshi et al. 2000, 2001; Fregeau et al. 2003; Fregeau & Rasio 2007; Chatterjee et al. 2010, 2013; Umbreit et al. 2012; Morscher et al. 2013; Rodriguez et al. 2018a; Kremer et al. 2020), Fewbody (Fregeau et al. 2004), COSMIC (Breivik et al. 2020).

Appendix

We include in this appendix the complete collision history for several BHs formed in our simulations. Tables 4–6 show histories for the three outcomes shown in Figures 2 and 3. Tables 7–9 show histories for the collisional runaways that occur in simulations 1a, 1b, and 1c. Note that in columns 3–5 of these tables, star type (k) of 0 refers to deeply or fully convective low-mass ($M \leq 0.7 M_{\odot}$) main-sequence stars, $k = 1$ refers to main-sequence stars with $M > 0.7 M_{\odot}$, $k = 4$ refers to core helium burning stars, and $k = 5$ refers to stars on the first asymptotic giant branch (all following the nomenclature of SSE; Hurley et al. 2000).

Table 4
Collision History for IMBH; Simulation 2c

	Time (Myr)	k_1	k_2	k_3	M_1	M_2 (M_{\odot})	M_3	$M_{\text{core},1}$	$M_{\text{core},2}$ (M_{\odot})	$M_{\text{core},3}$	b (R_{\odot})	v_{∞} (km s^{-1})
1	3.402	1	4	4	74.2	78.0	151.8	0.0	45.8	45.8	16593.1	45.0
2	3.619	1	4	4	59.3	119.0	177.9	0.0	47.3	47.3	16148.1	44.9
3	3.663	4	4	4	68.6	172.0	240.0	46.2	47.6	93.9	13960.6	38.7
4	3.689	4	4	4	70.7	236.0	305.8	41.6	94.3	135.9	139652.0	7.8
5	3.718	1	4	4	60.3	302.0	361.7	0.0	136.5	136.5	70966.5	20.7
6	3.772	1	4	4	18.0	353.0	370.8	0.0	137.9	137.9	12204.0	31.8
7	3.816	1	4	4	1.2	365.0	366.5	0.0	138.7	138.7	22870.3	53.3
8	3.823	1	4	4	1.8	365.0	366.9	0.0	138.9	138.9	12629.0	77.2
9	3.834	0	5	5	0.4	365.0	365.0	0.0	139.1	139.1	50813.6	59.1
10	3.834	14	328.1					

Note. Collision history for the $328.1 M_{\odot}$ IMBH shown in Figure 2. The numbers in column 1 correspond to the numbered events shown in Figure 3. k_1 , k_2 , and k_3 (columns 3–5) denote the stellar types (adopting the labeling scheme of SSE; Hurley et al. 2000) of the two collision inputs and the collision product, respectively. Columns 6–8 show the total stellar masses of the three stars and columns 9–11 show the core masses. Columns 12 and 13 show the impact parameter and velocity at infinity for the two colliding stars.

Table 5
Collision History for Pair-instability BHs; Simulation 2c

Time (Myr)	k_1	k_2	k_3	M_1	M_2 (M_\odot)	M_3	$M_{\text{core},1}$	$M_{\text{core},2}$ (M_\odot)	$M_{\text{core},3}$	b (R_\odot)	v_∞ (km s^{-1})	
1	3.228	1	1	1	0.9	88.0	89.2	0.0	0.0	0.0	254.6	76.1
2	3.757	0	4	4	0.2	66.0	66.3	0.0	42.0	42.0	2216.0	68.0
3	3.799	1	4	4	47.9	60.0	107.4	0.0	42.3	42.3	19816.0	24.2
4	3.999	14	69.9					

Note. Collision history for the 69.9 M_\odot BH show in Figure 2.

Table 6
PISN Collision History; Simulation 2c

Time (Myr)	k_1	k_2	k_3	M_1	M_2 (M_\odot)	M_3	$M_{\text{core},1}$	$M_{\text{core},2}$ (M_\odot)	$M_{\text{core},3}$	b (R_\odot)	v_∞ (km s^{-1})	
1	2.059	1	1	1	66.8	120.1	186.9	0.0	0.0	0.0	812.4	43.2
2	3.497	4	4	4	83.0	93.0	175.4	46.2	45.1	91.3	22794.8	33.8
3	3.606	0	4	4	0.1	159.0	158.8	0.0	93.0	93.0	18220.9	75.0
4	3.736	1	4	4	68.3	140.0	207.5	0.0	95.0	95.0	43961.7	24.7
5	3.742	1	4	4	0.9	207.0	207.5	0.0	95.0	95.0	11824.2	67.9
6	3.742	15	0.0					

Note. Collision history for the PISN show in Figure 2.

Table 7
Collision History for Runaway in Simulation 1a

Time (Myr)	k_1	k_2	k_3	M_1	M_2 (M_\odot)	M_3	$M_{\text{core},1}$	$M_{\text{core},2}$ (M_\odot)	$M_{\text{core},3}$	b (R_\odot)	v_∞ (km s^{-1})	
1	3.349	4	1	4	91.4	92.0	183.1	45.4	0.0	45.4	26727.3	25.9
2	3.491	4	4	4	78.2	161.0	239.2	46.2	46.4	92.6	35007.0	31.1
3	3.497	1	4	4	7.7	238.0	246.1	0.0	92.7	92.7	16795.6	71.8
4	3.519	4	4	4	90.0	243.0	331.9	45.7	93.0	138.7	59561.7	21.4
5	3.522	0	4	4	0.4	331.0	331.8	0.0	138.8	138.8	21606.0	68.0
6	3.524	1	4	4	31.5	332.0	362.8	0.0	138.8	138.8	85056.5	14.8
7	3.559	1	4	4	2.9	358.0	360.4	0.0	139.7	139.7	15062.1	72.7
8	3.563	4	4	4	178.2	360.0	537.3	46.8	139.8	186.6	156524.0	13.0
9	3.565	4	4	4	65.4	537.0	601.5	46.8	186.7	233.5	62288.0	37.0
10	3.567	1	4	4	25.4	601.0	626.3	0.0	233.6	233.6	133810.0	15.2
11	3.592	1	4	4	4.4	623.0	626.9	0.0	234.6	234.6	32677.6	80.6
12	3.593	1	4	4	4.9	627.0	631.5	0.0	234.6	234.6	61943.9	41.2
13	3.613	4	4	4	80.8	628.0	708.4	41.6	235.5	277.1	73274.9	23.6
14	3.614	0	4	4	0.2	708.0	708.4	0.0	277.1	277.1	29014.8	82.2
15	3.619	1	4	4	25.3	708.0	732.7	0.0	277.3	277.3	35068.2	23.9
16	3.62	4	4	4	695.7	733.0	1426.8	139.3	277.4	416.7	224846.0	11.6





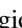
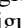


Table 8
Collision History for Runaway in Simulation 1b

	Time (Myr)	k_1	k_2	k_3	M_1	M_2 (M_\odot)	M_3	$M_{\text{core},1}$	$M_{\text{core},2}$ (M_\odot)	$M_{\text{core},3}$	b (R_\odot)	v_∞ (km s^{-1})
1	3.352	4	4	4	92.8	95.0	187.2	45.5	45.4	90.9	22096.2	49.4
2	3.41	1	4	4	47.8	178.0	225.7	0.0	91.8	91.8	50954.1	17.3
3	3.472	4	4	4	123.1	216.0	338.5	46.6	92.8	139.4	56550.8	24.5
4	3.5	1	4	4	7.3	334.0	341.5	0.0	140.0	140.0	20029.7	77.0
5	3.527	1	4	4	3.2	337.0	340.6	0.0	140.7	140.7	59184.8	18.9
6	3.535	1	4	4	87.4	339.0	426.5	0.0	140.9	140.9	4208.3	73.6
7	3.541	1	4	4	2.4	426.0	428.0	0.0	141.0	141.0	44744.4	26.2
8	3.545	1	4	4	13.6	427.0	440.9	0.0	141.1	141.1	70184.8	18.3
9	3.548	1	4	4	56.7	440.0	497.0	0.0	141.2	141.2	18116.4	68.3
10	3.569	4	4	4	444.6	494.0	936.5	185.9	141.7	327.6	37210.6	19.0
11	3.571	1	4	4	59.1	936.0	995.1	0.0	327.8	327.8	150765.0	15.1
12	3.574	1	4	4	21.2	995.0	1015.7	0.0	327.9	327.9	190181.0	16.1

Table 9
Collision History for Runaway in Simulation 1c

	Time (Myr)	k_1	k_2	k_3	M_1	M_2 (M_\odot)	M_3	$M_{\text{core},1}$	$M_{\text{core},2}$ (M_\odot)	$M_{\text{core},3}$	b (R_\odot)	v_∞ (km s^{-1})
1	3.446	4	4	4	82.3	93.0	174.3	45.6	45.3	90.9	27762.1	29.3
2	3.488	1	4	4	3.2	168.0	171.2	0.0	91.6	91.6	9218.1	81.3
3	3.546	1	4	4	59.6	162.0	221.6	0.0	92.5	92.5	36207.6	21.8
4	3.572	1	4	4	52.8	218.0	270.2	0.0	92.9	92.9	22892.2	49.4
5	3.59	4	4	4	85.1	268.0	352.0	41.0	93.1	134.2	117451.0	13.3
6	3.622	1	4	4	8.4	347.0	355.4	0.0	134.9	134.9	19602.9	50.3
7	3.702	4	4	4	147.6	343.0	490.4	40.9	136.8	177.6	38033.3	37.3
8	3.704	4	4	4	363.3	490.0	851.0	143.2	177.7	320.9	102791.0	34.0
9	3.706	1	4	4	57.4	851.0	907.0	0.0	321.1	321.1	39229.5	37.6
10	3.709	1	4	4	19.6	907.0	926.7	0.0	321.3	321.3	837690.0	3.8
11	3.71	4	4	4	550.5	927.0	1474.9	144.2	321.3	465.5	380430.0	6.7

ORCID iDs

Kyle Kremer  <https://orcid.org/0000-0002-4086-3180>
 Mario Spera  <https://orcid.org/0000-0003-0930-6930>
 Sourav Chatterjee  <https://orcid.org/0000-0002-3680-2684>
 Ugo N. Di Carlo  <https://orcid.org/0000-0003-2654-5239>
 Giacomo Fragione  <https://orcid.org/0000-0002-7330-027X>
 Carl L. Rodriguez  <https://orcid.org/0000-0003-4175-8881>
 Claire S. Ye  <https://orcid.org/0000-0001-9582-881X>
 Frederic A. Rasio  <https://orcid.org/0000-0002-7132-418X>

References

- Abbott, R., Abbott, T. D., Abraham, S., et al. 2020a, *ApJ*, 900, L13
 Abbott, R., Abbott, T. D., Abraham, S., et al. 2020b, *PhRvL*, 125, 101102
 Amaro-Seoane, P., Gair, J. R., Freitag, M., et al. 2007, *CQGra*, 24, R113
 Antonini, F., & Gieles, M. 2020, *MNRAS*, 492, 2936
 Antonini, F., & Rasio, F. A. 2016, *ApJ*, 831, 187
 Antonini, F., Toonen, S., & Hamers, A. S. 2017, *ApJ*, 841, 77
 Arca Sedda, M., Askar, A., & Giersz, M. 2018, *MNRAS*, 479, 4652
 Ardi, E., Baumgardt, H., & Mineshige, S. 2008, *ApJ*, 682, 1195
 Askar, A., Szkudlarek, M., Gondek-Rosińska, D., Giersz, M., & Bulik, T. 2017, *MNRAS*, 464, L36
 Bailyn, C. D., Jain, R. K., Coppi, P., & Orosz, J. A. 1998, *ApJ*, 499, 367
 Banerjee, S. 2018, *MNRAS*, 473, 909
 Banerjee, S. 2020, *MNRAS*, staa2392
 Banerjee, S., Baumgardt, H., & Kroupa, P. 2010, *MNRAS*, 402, 371
 Barausse, E., & Rezzolla, L. 2009, *ApJ*, 704, L40
 Barkat, Z., Rakavy, G., & Sack, N. 1967, *PhRvL*, 18, 379
 Bastian, N., Covey, K. R., & Meyer, M. R. 2010, *ARA&A*, 48, 339
 Batta, A., & Ramirez-Ruiz, E. 2019, arXiv:1904.04835
 Baumgardt, H., De Marchi, G., & Kroupa, P. 2008, *ApJ*, 685, 247
 Baumgardt, H., & Hilker, M. 2018, *MNRAS*, 478, 1520
 Belczynski, K., Bulik, T., Fryer, C. L., et al. 2010, *ApJ*, 714, 1217
 Belczynski, K., Heger, A., Gladysz, W., et al. 2016a, *A&A*, 594, A97
 Belczynski, K., Hirschi, R., Kaiser, E. A., et al. 2020, *ApJ*, 890, 113
 Belczynski, K., Holz, D. E., Bulik, T., & O’Shaughnessy, R. 2016b, *Natur*, 534, 512
 Berti, E., Cardoso, V., Gonzalez, J. A., et al. 2007, *PhRvD*, 76, 064034
 Bird, S., Cholis, I., Muñoz, J. B., et al. 2016, *PhRvL*, 116, 201301
 Bond, J. R., Arnett, W. D., & Carr, B. J. 1984, *ApJ*, 280, 825
 Bonnell, I. A., & Bate, M. R. 2006, *MNRAS*, 370, 488
 Breen, P. G., & Heggie, D. C. 2013, *MNRAS*, 432, 2779
 Breivik, K., Coughlin, S., Zevin, M., et al. 2020, *ApJ*, 898, 71
 Bromm, V., & Loeb, A. 2003, *Natur*, 425, 812
 Campanelli, M., Lousto, C. O., Zlochower, Y., & Merritt, D. 2007, *PhRvL*, 98, 231102
 Carr, B., Kühnel, F., & Sandstad, M. 2016, *PhRvD*, 94, 083504
 Cartwright, A., & Whitworth, A. P. 2004, *MNRAS*, 348, 589
 Chatterjee, S., Fregeau, J. M., Umbreit, S., & Rasio, F. A. 2010, *ApJ*, 719, 915
 Chatterjee, S., Goswami, S., Umbreit, S., et al. 2009, arXiv:0911.1483
 Chatterjee, S., Rodriguez, C. L., Kalogera, V., & Rasio, F. A. 2017a, *ApJL*, 836, L26
 Chatterjee, S., Rodriguez, C. L., & Rasio, F. A. 2017b, *ApJ*, 834, 68
 Chatterjee, S., Umbreit, S., Fregeau, J. M., & Rasio, F. A. 2013, *MNRAS*, 429, 2881
 Chatzopoulos, E., & Wheeler, J. C. 2012, *ApJ*, 748, 42
 Chen, Y., Bressan, A., Girardi, L., et al. 2015, *MNRAS*, 452, 1068
 Chomiuk, L., Strader, J., Maccarone, T. J., et al. 2013, *ApJ*, 777, 69
 Cooke, J., Sullivan, M., Gal-Yam, A., et al. 2012, *Natur*, 491, 228
 Corral-Santana, J. M., Casares, J., Muñoz-Darias, T., et al. 2016, *A&A*, 587, A61
 Dessart, L., Waldman, R., Livne, E., Hillier, D. J., & Blondin, S. 2013, *MNRAS*, 428, 3227

- Di Carlo, U. N., Giacobbo, N., Mapelli, M., et al. 2019, *MNRAS*, **487**, 2947
- Di Carlo, U. N., Mapelli, M., Bouffanais, Y., et al. 2020, *MNRAS*, **497**, 1043
- Dominik, M., Belczynski, K., Fryer, C., et al. 2012, *ApJ*, **759**, 52
- Dominik, M., Belczynski, K., Fryer, C., et al. 2013, *ApJ*, **779**, 72
- D’Orazio, D. J., & Samsing, J. 2018, *MNRAS*, **481**, 4775
- Ebisuzaki, T., Makino, J., Tsuru, T. G., et al. 2001, *ApJL*, **562**, L19
- El-Badry, K., Quataert, E., Weisz, D. R., Choksi, N., & Boylan-Kolchin, M. 2019, *MNRAS*, **482**, 4528
- Ertl, T., Janka, H. T., Woosley, S. E., Sukhbold, T., & Ugliano, M. 2016, *ApJ*, **818**, 124
- Farmer, R., Renzo, M., de Mink, S. E., Marchant, P., & Justham, S. 2019, *ApJ*, **887**, 53
- Farr, W. M., Sravan, N., Cantrell, A., et al. 2011, *ApJ*, **741**, 103
- Feldmeier, A., Lützgendorf, N., Neumayer, N., et al. 2013, *A&A*, **554**, A63
- Figer, D. F. 2005, *Natur*, **434**, 192
- Fischer, P., Pryor, C., Murray, S., Mateo, M., & Richtler, T. 1998, *AJ*, **115**, 592
- Fishbach, M., & Holz, D. E. 2017, *ApJL*, **851**, L25
- Fowler, W. A., & Hoyle, F. 1964, *ApJS*, **9**, 201
- Fragione, G., Ginsburg, I., & Kocsis, B. 2018a, *ApJ*, **856**, 92
- Fragione, G., Grishin, E., Leigh, N. W. C., Perets, H. B., & Perna, R. 2019a, *MNRAS*, **488**, 47
- Fragione, G., & Kocsis, B. 2018, *PhRvL*, **121**, 161103
- Fragione, G., & Kocsis, B. 2019, *MNRAS*, **486**, 4781
- Fragione, G., Leigh, N. W. C., Ginsburg, I., & Kocsis, B. 2018b, *ApJ*, **867**, 119
- Fragione, G., Leigh, N. W. C., & Perna, R. 2019b, *MNRAS*, **488**, 2825
- Fragione, G., Loeb, A., Kremer, K., & Rasio, F. A. 2020, *ApJ*, **897**, 46
- Fragos, T., & McClintock, J. E. 2015, *ApJ*, **800**, 17
- Fraley, G. S. 1968, *Ap&SS*, **2**, 96
- Fregeau, J. M., Cheung, P., Portegies Zwart, S. F., & Rasio, F. A. 2004, *MNRAS*, **352**, 1
- Fregeau, J. M., Gurkan, M. A., Joshi, K. J., & Rasio, F. A. 2003, *ApJ*, **593**, 772
- Fregeau, J. M., & Rasio, F. A. 2007, *ApJ*, **658**, 1047
- Freitag, M., Gürkan, M. A., & Rasio, F. A. 2006, *MNRAS*, **368**, 141
- Fryer, C. L., Belczynski, K., Wiktorowicz, G., et al. 2012, *ApJ*, **749**, 91
- Fryer, C. L., Woosley, S. E., & Heger, A. 2001, *ApJ*, **550**, 372
- Fuller, J., & Ma, L. 2019, *ApJL*, **881**, L1
- Gaburov, E., Lombardi, J. C. J., & Portegies Zwart, S. 2010, *MNRAS*, **402**, 105
- Gal-Yam, A., Mazzali, P., Ofek, E. O., et al. 2009, *Natur*, **462**, 624
- Gerosa, D., & Berti, E. 2019, *PhRvD*, **100**, 041301
- Gerosa, D., & Kesden, M. 2016, *PhRvD*, **93**, 124066
- Giacobbo, N., Mapelli, M., & Spera, M. 2018, *MNRAS*, **474**, 2959
- Gieles, M., Balbinot, E., Yaaqib, R. I. S. M., et al. 2018, *MNRAS*, **473**, 4832
- Giersz, M., Leigh, N., Hypki, A., Lützgendorf, N., & Askar, A. 2015, *MNRAS*, **454**, 3150
- Giesers, B., Dreizler, S., Husser, T.-O., et al. 2018, *MNRAS*, **475**, L15
- Giesers, B., Kamann, S., Dreizler, S., et al. 2019, *A&A*, **632**, A3
- Glebbeeck, E., Gaburov, E., de Mink, S. E., Pols, O. R., & Portegies Zwart, S. F. 2009, *A&A*, **497**, 255
- Gnedin, O. Y., Ostriker, J. P., & Tremaine, S. 2014, *ApJ*, **785**, 71
- Gomez, S., Berger, E., Nicholl, M., et al. 2019, *ApJ*, **881**, 87
- González, J. A., Spherhake, U., Brüggemann, B., Hannam, M., & Husa, S. 2007, *PhRvL*, **98**, 091101
- Goswami, S., Umbreit, S., Bierbaum, M., & Rasio, F. A. 2012, *ApJ*, **752**, 43
- Gouliermis, D., Keller, S. C., Kontizas, M., Kontizas, E., & Bellas-Velidis, I. 2004, *A&A*, **416**, 137
- Greene, J. E., Strader, J., & Ho, L. C. 2019, arXiv:1911.09678
- Gürkan, M. A., Fregeau, J. M., & Rasio, F. A. 2006, *ApJL*, **640**, L39
- Gürkan, M. A., Freitag, M., & Rasio, F. A. 2004, *ApJ*, **604**, 632
- Gutermuth, R. A., Megeath, S. T., Pipher, J. L., et al. 2005, *ApJ*, **632**, 397
- Harris, W. E. 1996, *AJ*, **112**, 1487
- Heger, A., Fryer, C. L., Woosley, S. E., Langer, N., & Hartmann, D. H. 2003, *ApJ*, **591**, 288
- Heger, A., & Woosley, S. E. 2002, *ApJ*, **567**, 532
- Heger, A., Woosley, S. E., & Spruit, H. C. 2005, *ApJ*, **626**, 350
- Heggie, D., & Hut, P. 2003, *The Gravitational Million-Body Problem: A Multidisciplinary Approach to Star Cluster Dynamics* (Cambridge: Cambridge Univ. Press)
- Hillenbrand, L. A. 1997, *AJ*, **113**, 1733
- Hillenbrand, L. A., & Hartmann, L. W. 1998, *ApJ*, **492**, 540
- Hoang, B.-M., Naoz, S., Kocsis, B., Rasio, F. A., & Dosopoulou, F. 2018, *ApJ*, **856**, 140
- Hurley, J. R., Pols, O. R., & Tout, C. A. 2000, *MNRAS*, **315**, 543
- Hurley, J. R., Tout, C. A., & Pols, O. R. 2002, *MNRAS*, **329**, 897
- Joshi, K. J., Nave, C. P., & Rasio, F. A. 2001, *ApJ*, **550**, 691
- Joshi, K. J., Rasio, F. A., Zwart, S. P., & Portegies Zwart, S. 2000, *ApJ*, **540**, 969
- Kasen, D., Woosley, S. E., & Heger, A. 2011, *ApJ*, **734**, 102
- Katz, H., Sijacki, D., & Haehnelt, M. G. 2015, *MNRAS*, **451**, 2352
- Kozyreva, A., Blinnikov, S., Langer, N., & Yoon, S. C. 2014, *A&A*, **565**, A70
- Kremer, K., Chatterjee, S., Ye, C. S., Rodriguez, C. L., & Rasio, F. A. 2019, *ApJ*, **871**, 38
- Kremer, K., Ye, C. S., Chatterjee, S., Rodriguez, C. L., & Rasio, F. A. 2018, *ApJL*, **855**, L15
- Kremer, K., Ye, C. S., Rui, N. Z., et al. 2020, *ApJS*, **247**, 48
- Kroupa, P. 2001, *MNRAS*, **322**, 231
- Langer, N., Norman, C. A., de Koter, A., et al. 2007, *A&A*, **475**, L19
- Leigh, N. W. C., Geller, A. M., McKernan, B., et al. 2018, *MNRAS*, **474**, 5672
- Limongi, M., & Chieffi, A. 2018, *ApJS*, **237**, 13
- Liu, B., & Lai, D. 2017, *ApJL*, **846**, L11
- Lombardi, J. C. J., Warren, J. S., Rasio, F. A., Sills, A., & Warren, A. R. 2002, *ApJ*, **568**, 939
- Lousto, C. O., & Zlochower, Y. 2008, *PhRvD*, **77**, 044028
- Lousto, C. O., & Zlochower, Y. 2013, *PhRvD*, **87**, 084027
- Lousto, C. O., Zlochower, Y., Dotti, M., & Volonteri, M. 2012, *PhRvD*, **85**, 084015
- Lovegrove, E., & Woosley, S. E. 2013, *ApJ*, **769**, 109
- Lützgendorf, N., Kissler-Patig, M., Noyola, E., et al. 2011, *A&A*, **533**, A36
- Mackey, A. D., Wilkinson, M. I., Davies, M. B., & Gilmore, G. F. 2007, *MNRAS*, **379**, L40
- Mackey, A. D., Wilkinson, M. I., Davies, M. B., & Gilmore, G. F. 2008, *MNRAS*, **386**, 65
- MacLeod, M., Goldstein, J., Ramirez-Ruiz, E., Guillochon, J., & Samsing, J. 2014, *ApJ*, **794**, 9
- MacLeod, M., Trenti, M., & Ramirez-Ruiz, E. 2016, *ApJ*, **819**, 70
- Mandel, I., Brown, D. A., Gair, J. R., & Miller, M. C. 2008, *ApJ*, **681**, 1431
- Mapelli, M. 2016, *MNRAS*, **459**, 3432
- Mapelli, M., Ripamonti, E., Zampieri, L., Colpi, M., & Bressan, A. 2010, *MNRAS*, **408**, 234
- Mapelli, M., Spera, M., Montanari, E., et al. 2020, *ApJ*, **888**, 76
- Marchant, P., Renzo, M., Farmer, R., et al. 2019, *ApJ*, **882**, 36
- María Ezquiaga, J., & Holz, D. E. 2020, arXiv:2006.02211
- Marks, M., Kroupa, P., Dabringhausen, J., & Pawlowski, M. S. 2012, *MNRAS*, **422**, 2246
- McKernan, B., Ford, K. E. S., Lyra, W., & Perets, H. B. 2012, *MNRAS*, **425**, 460
- McKernan, B., Ford, K. E. S., O’Shaughnessy, R., & Wysocki, D. 2020, *MNRAS*, **494**, 1203
- Merritt, D., Piatek, S., Portegies Zwart, S., & Hensendorf, M. 2004, *ApJL*, **608**, L25
- Miller, M. C., & Hamilton, D. P. 2002, *MNRAS*, **330**, 232
- Miller, M. C., & Miller, J. M. 2015, *PhR*, **548**, 1
- Miller-Jones, J. C. A., Strader, J., Heinke, C. O., et al. 2015, *MNRAS*, **453**, 3918
- Morscher, M., Pattabiraman, B., Rodriguez, C., Rasio, F. A., & Umbreit, S. 2015, *ApJ*, **800**, 9
- Morscher, M., Umbreit, S., Farr, W. M., & Rasio, F. A. 2013, *ApJL*, **763**, L15
- Murray, S. D., & Lin, D. N. C. 1996, *ApJ*, **467**, 728
- Nicholl, M., Blanchard, P. K., Berger, E., et al. 2020, *NatAs*, **4**, 893
- Noyola, E., Gebhardt, K., Kissler-Patig, M., et al. 2010, *ApJL*, **719**, L60
- O’Connor, E., & Ott, C. D. 2011, *ApJ*, **730**, 70
- O’Leary, R. M., Kocsis, B., & Loeb, A. 2009, *MNRAS*, **395**, 2127
- Özel, F., Psaltis, D., Narayan, R., & McClintock, J. E. 2010, *ApJ*, **725**, 1918
- Pan, T., Loeb, A., & Kasen, D. 2012, *MNRAS*, **423**, 2203
- Paxton, B., Marchant, P., Schwab, J., et al. 2015, *ApJS*, **220**, 15
- Perera, B. B. P., Stappers, B. W., Lyne, A. G., et al. 2017, *MNRAS*, **468**, 2114
- Peuten, M., Zocchi, A., Gieles, M., Gualandris, A., & Hénault-Brunet, V. 2016, *MNRAS*, **462**, 2333
- Portegies Zwart, S. F., Baumgardt, H., Hut, P., Makino, J., & McMillan, S. L. W. 2004, *Natur*, **428**, 724
- Portegies Zwart, S. F., & Mcmillan, S. L. W. 2000, *ApJ*, **528**, 17
- Portegies Zwart, S. F., & McMillan, S. L. W. 2002a, *ApJ*, **576**, 899
- Portegies Zwart, S. F., & McMillan, S. L. W. 2002b, *ApJ*, **576**, 899
- Portegies Zwart, S. F., McMillan, S. L. W., & Gieles, M. 2010, *ARA&A*, **48**, 431
- Portegies Zwart, S. F., & van den Heuvel, E. P. J. 2007, *Natur*, **450**, 388
- Qin, Y., Marchant, P., Fragos, T., Meynet, G., & Kalogera, V. 2019, *ApJL*, **870**, L18
- Rakavy, G., & Shaviv, G. 1967, *ApJ*, **148**, 803
- Renzo, M., Farmer, R., Justham, S., et al. 2020, *A&A*, **640**, A56

- Rodriguez, C. L., Amaro-Seoane, P., Chatterjee, S., et al. 2018a, *PhRvD*, **98**, 123005
- Rodriguez, C. L., Amaro-Seoane, P., Chatterjee, S., & Rasio, F. A. 2018b, *PhRvL*, **120**, 151101
- Rodriguez, C. L., & Antonini, F. 2018, *ApJ*, **863**, 7
- Rodriguez, C. L., Chatterjee, S., & Rasio, F. A. 2016, *PhRvD*, **93**, 084029
- Rodriguez, C. L., & Loeb, A. 2018, *ApJL*, **866**, L5
- Rodriguez, C. L., Morscher, M., Pattabiraman, B., et al. 2015, *PhRvL*, **115**, 051101
- Rodriguez, C. L., Zevin, M., Amaro-Seoane, P., et al. 2019, *PhRvD*, **100**, 043027
- Rosswog, S., Ramirez-Ruiz, E., & Hix, W. R. 2009, *ApJ*, **695**, 404
- Samsing, J., & D’Orazio, D. J. 2018, *MNRAS*, **481**, 5445
- Samsing, J., D’Orazio, D. J., Askar, A., & Giersz, M. 2018, arXiv:1802.08654
- Sasaki, M., Suyama, T., Tanaka, T., & Yokoyama, S. 2016, *PhRvL*, **117**, 061101
- Schneider, F. R. N., Sana, H., Evans, C. J., et al. 2018, *Sci*, **359**, 69
- Secunda, A., Bellovary, J., Mac Low, M.-M., et al. 2019, *ApJ*, **878**, 85
- Shishkovsky, L., Strader, J., Chomiuk, L., et al. 2018, *ApJ*, **855**, 55
- Silber, K., & Tremaine, S. 2017, *ApJ*, **836**, 39
- Smith, N., Li, W., Foley, R. J., et al. 2007, *ApJ*, **666**, 1116
- Spera, M., & Mapelli, M. 2017, *MNRAS*, **470**, 4739
- Spera, M., Mapelli, M., & Bressan, A. 2015, *MNRAS*, **451**, 4086
- Spera, M., Mapelli, M., Giacobbo, N., et al. 2019, *MNRAS*, **485**, 889
- Spitzer, L. 1987, *Dynamical Evolution of Globular Clusters* (Princeton, NJ: Princeton Univ. Press)
- Stevenson, S., Sampson, M., Powell, J., et al. 2019, *ApJ*, **882**, 121
- Stolte, A., Brandner, W., Brandl, B., & Zinnecker, H. 2006, *AJ*, **132**, 253
- Strader, J., Chomiuk, L., Maccarone, T. J., Miller-Jones, J. C. A., & Seth, A. C. 2012, *Natur*, **490**, 71
- Sukhbold, T., Ertl, T., Woosley, S. E., Brown, J. M., & Janka, H. T. 2016, *ApJ*, **821**, 38
- Talbot, C., & Thrane, E. 2018, *ApJ*, **856**, 173
- Terreran, G., Pumo, M. L., Chen, T. W., et al. 2017, *NatAs*, **1**, 713
- The LIGO Scientific Collaboration/Virgo Collaboration, Abbott, B. P., et al. 2019a, *ApJL*, **882**, L24
- The LIGO Scientific Collaboration/Virgo Collaboration, Abbott, B. P., et al. 2019b, *PhRvX*, **9**, 031040
- Tremou, E., Strader, J., Chomiuk, L., et al. 2018, *ApJ*, **862**, 16
- Umbreit, S., Fregeau, J. M., Chatterjee, S., & Rasio, F. A. 2012, *ApJ*, **750**, 31
- Vink, J. S., de Koter, A., & Lamers, H. J. G. L. M. 2001, *A&A*, **369**, 574
- Wang, L., Spurzem, R., Aarseth, S., et al. 2015, *MNRAS*, **450**, 4070
- Wang, L., Spurzem, R., Aarseth, S., et al. 2016, *MNRAS*, **458**, 1450
- Weatherford, N. C., Chatterjee, S., Kremer, K., & Rasio, F. A. 2020, *ApJ*, **898**, 162
- Weatherford, N. C., Chatterjee, S., Rodriguez, C. L., & Rasio, F. A. 2018, *ApJ*, **864**, 13
- Weidner, C., Kroupa, P., & Bonnell, I. A. D. 2010, *MNRAS*, **401**, 275
- Woosley, S. E. 2017, *ApJ*, **836**, 244
- Woosley, S. E. 2019, *ApJ*, **878**, 49
- Woosley, S. E., Blinnikov, S., & Heger, A. 2007, *Natur*, **450**, 390
- Yang, Y., Bartos, I., Haiman, Z., et al. 2019, *ApJ*, **876**, 122
- Yungelson, L. R., van den Heuvel, E. P. J., Vink, J. S., Portegies Zwart, S. F., & de Koter, A. 2008, *A&A*, **477**, 223
- Zevin, M., Samsing, J., Rodriguez, C., Haster, C.-J., & Ramirez-Ruiz, E. 2019, *ApJ*, **871**, 91
- Ziosi, B. M., Mapelli, M., Branchesi, M., & Tormen, G. 2014, *MNRAS*, **441**, 3703
- Zocchi, A., Gieles, M., & Hénault-Brunet, V. 2019, *MNRAS*, **482**, 4713